Europium induced point defects in SrSnO3-based perovskites employed as antibacterial agents

L. Chantelle, B.J. Kennedy, C.P. de Oliveira, F Gouttefangeas, M. Siu-Li, R. Landers, A. Ciorita, A.M. Rostas, I.M.G. dos Santos, A.L. Menezes de Oliveira

Europium induced point defects in $SrSnO_3$-based perovskites employed as antibacterial agents.

Laís Chantelle,[a] Brendan James Kennedy,[b] Cybelle Pereira de Oliveira,[c] Francis Gouttefangeas,[d] Máximo Siu-Li,[e] Richard Landers,[f] Alexandra Ciorita,[g] Arpad Mihai Rostas,[g,**] Iêda Maria Garcia dos Santos,[a] and André Luiz Menezes de Oliveira,[a,b,*]

[a]*NPE-LACOM, Dept. de Química, Universidade Federal da Paraíba, João Pessoa, PB 58051-085, Brazil.*

[b]*School of Chemistry, The University of Sydney, Sydney, NSW 2006, Australia.*

[c]*Dept. de Gestão e Tecnologia Agroindustrial, Universidade Federal da Paraíba, CCHSA, Bananeiras, PB 58220-000, Brazil.*

[d]*Institutes des Sciences Chimiques de Rennes, Université de Rennes, Rennes, F-35000, France.*

[e]*Instituto de Física, Universidade de São Paulo, São Carlos, SP 13563-120, Brazil.*

[f]*Instituto de Física Gleb Wataghin, Universidade Estadual de Campinas, Campinas, SP 13083-859, Brazil.*

[g]*National Institute for Research and Development of Isotopic and Molecular Technologies, Cluj-Napoca, 400293, Romania.*

*** Corresponding author** (A.L.M.O.)

E-mail address: andrel_ltm@hotmail.com

**** Corresponding author** (A.M.R.)

E-mail addresses: arpad.rostas@itim-cj.ro

ABSTRACT.

The antibacterial activity of Eu^{3+}-doped $SrSnO_3$-type materials against *Staphylococcus aureus* (Gram-positive) and *Escherichia coli* (Gram-negative) bacteria is described. Two Eu^{3+}-doped $SrSnO_3$ perovskites - $(SrEu)SnO_3$ and $Sr(SnEu)O_3$ - were synthesised by a modified-Pechini method and characterised by XRD, FT-IR, FE-SEM, HR-STEM/EDX, BET, Photoluminescence (PL), UV-Vis, Q-band EPR and XPS to understand the impact of Eu doping on the materials' properties. Structural characterisations indicated that the desired perovskite phase completely crystallised after calcination at 700 °C. Long and short-range structural changes were observed as a function of the site-doping with Eu and calcination temperature. Small specific surface area, which varied from 8.09 to 13.28 m^2/g, was observed for the samples. Nonetheless, the formation of nanoparticles under 10 nm, clusters of nanoparticles > 100 nm, and nanorods with 100 - 600 nm × 10-50 nm (length × width) was evidenced. Eu^{3+} doping led to an increase of Sn^{2+} and oxygen vacancies in $SrSnO_3$ lattice, playing an essential role in the antibacterial activity. Reduced Eu^{2+} species were also observed. The samples had activity below 5% against *Escherichia coli*, whereas $(SrEu)SnO_3$ displayed an efficiency of 100% after 24 h against *Staphylococcus aureus* at a concentration of 1 mg/mL. Our results demonstrate that a specific chemical doping with Eu induces the formation of distinct point defect (Sn^{2+}, Eu^{2+} and $V_O^{\bullet}$) in the materials, which promoted a negative surface charge that seems to have improved the redox ability and, therefore, enhanced the biocide property.

Graphical abstract

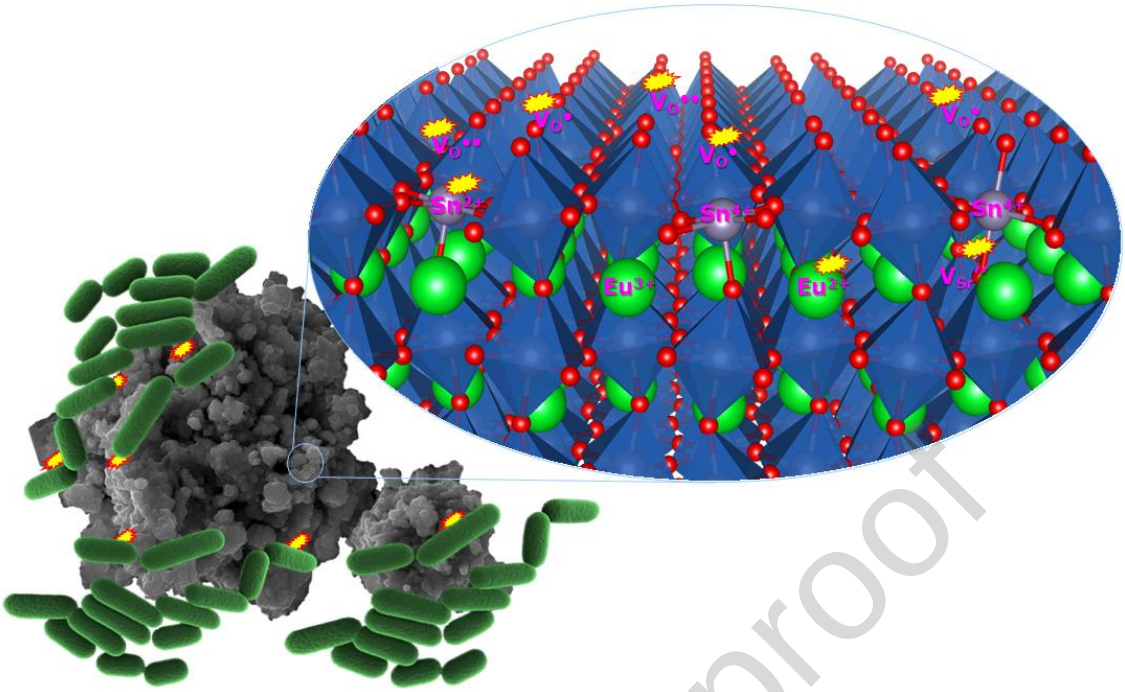

Keywords: $SrSnO_3$ perovskites; Europium; Antibacterial activity; EPR spectroscopy; XPS spectroscopy; Photoluminescence

1. Introduction

Pathogenic bacteria are a significant and increasing cause of chronic infections and mortality in humans due to bacterial multi-drug resistance to antibiotics and the host immune system. This leads to increased healthcare spending and a high risk to public health. Therefore, developing new antibacterial agents is extremely important [1, 2]. Nanoparticles as antibacterial agents have attracted considerable attention in the last few decades, widely used in biomedical fields [3].

Inorganic nanomaterials have emerged as promising antibacterial agents due to their low toxicity, high stability, and high selectivity compared to other chemical agents [4, 5]. For instance, nanoparticulate metal oxides, especially ZnO, TiO_2, SnO_2, and Fe_2O_3, have been widely applied for presenting different chemical, magnetic, mechanical, electrical, and optical properties, as a function of the various structures they may adopt [6, 7]. Moreover, the difference in efficacy of nanoparticle oxides is related to their large surface area and electronic defects on the surface, which allows efficient interaction with the bacteria [2, 8]. Thus, the materials can act by electrostatic interactions that alter bacterial cell walls. Materials can also generate reactive oxygen

species (ROS) on the surface and enter the microorganism, damaging the enzymatic pathways or the bacteria DNA [9]. The mechanism of nanoparticles as antibacterial agents depends mainly on their material chemistry. Still, it strongly correlates with nanoparticle properties such as shape, size, solubility, agglomeration, and surface charge properties [10].

The use of perovskite oxide-based nanoparticles has recently attracted increased attention for different technological applications, including biological and medical fields such as antibacterial, antifungal, and antiviral [6, 11]. Among different oxides with perovskite structure, alkaline-earth stannates ($MSnO_3$, M = Ca, Ba, and Sr) need to be highlighted. Particularly, strontium stannate ($SrSnO_3$) has become one of the most promising explored perovskites for showing potential for applications in several fields, as in Li-ion batteries [12], gas/humidity [13, 14] and anti-inflammatory drug sensors [15], photocatalysis [16, 17, 18], luminescence [19], and antibacterial agents [20, 21], among others.

Concerning the applications as antibacterial agents, examples of some perovskites that have been applied against Gram-positive and Gram-negative bacteria [21, 22, 23, 24] can be provided. For instance, Shah et al. [23] synthesised barium titanate ($BaTiO_3$) nanoparticles and evaluated the effect of its structural and morphological properties on antibacterial and antibiofilm activity against *Pseudomonas aeruginosa* (*P. aeruginosa*) and *Staphylococcus aureus* (*S. aureus*). These authors used the disk diffusion method to show that $BaTiO_3$ presented considerable bacteria inhibition. $BaTiO_3$ also inhibited biofilm formation with 85 ± 3.5 % and 80 ± 3 % biofilms formed by *S. aureus* and *P. aeruginosa*, respectively. Singh et al. [24] investigated the antibacterial activity of lanthanum cobalt ferrite ($LaCo_{1-x}Fe_xO_3$) against P. aeruginosa and S. aureus. The authors observed that the minimum inhibitory concentration (MIC) values were between 50 and 200 mg/mL. The antibacterial activity increased by increasing the doping concentration. The authors also proposed that the likely mechanism was related to the nanoparticle's adsorption capacity due to the cationic charge on the surface, which resulted in enhanced interaction with the surface of Gram-negative bacterial cells. Subhan et al. [21] evaluated the antibacterial activity of $SrSnO_3$:Ag nanocomposites. The authors evidenced that 3 mg/mL of the synthesised nanocomposites killed Gram-positive and Gram-negative bacteria in the dark. In contrast, 1 and 2 mg/mL of the nanocomposites had good antibacterial activity while

irradiated with visible light using a tungsten lamp. In the presence of light, hole-electron pairs are generated on the irradiated materials, which, in contact with aqueous solutions, generate ROS that inhibit the bacteria growth [25].

Lanthanoid-based inorganic materials with potential use in life science, especially due to their anti-inflammatory, antitumor and antibacterial effects, have attracted major interest because of their physicochemical properties [26, 27, 28, 29, 30]. Lanthanoid metal ions can promote interesting electronic structures incorporated in different inorganic matrices due to their 4f electron configuration. Rare earth elements are also less expensive and less toxic than other elements with known antibacterial properties, for instance, Ag^{+}, which make them very useful in agriculture, health care and other fields [29]. It is also reported that adding rare earth in inorganic materials can improve antibacterial properties [20, 26, 27].

Despite different studies concerning rare earths-containing materials, few works dealing with lanthanoid, and lanthanoid-doped ABO_3-type perovskites have been reported [20, 24, 26]. For instance, Singh et al. [24] evaluated the antibacterial activity of Fe-doped $LaCoO_3$ perovskite nanoparticles against *S. aureaus*. Recently, Sudhaparimala [20] investigated the effect of europium content (0.2, 0.50, and 0.75 mol%) on the antibacterial activity of $MSnO_3$ (M = Ca and Ba) and reported that 50% cell toxicity was observed against *P. aeruginosa* and *S. aureus* when 600 μg of the inorganic solids were used compared to 500 μg of the control tetracycline.

In this context, our research focused, for the first time, on evaluating the antibacterial activity of a potential perovskite, $SrSnO_3$, and establishing the effect of surface structural and electronic defects created by doping with europium on the inhibition of *Escherichia coli (E. coli*) and *Staphylococcus aureus* (*S. aureus*) bacteria growth. *S. aureus* and *E. coli* were used as target microorganisms to evaluate the antibacterial effect of the synthesized materials because they are common highly infectious bacteria that cause the most illnesses and hospitalisations, besides tending to develop antibiotic resistance [31, 32]. *S. aureus* is a frequent coloniser of several parts of the human body, and their colonisation is the major risk for clinical infection [31]. *E. coli* is also part of the normal flora of humans. It also can be found in water and food, which can be harmful when ingested [32]. In addition, these two bacteria present different cell wall characteristics. Gram-negative bacteria have a lipopolysaccharide cell

wall with a high amount of carboxylic groups and a thinner layer of the peptidoglycan instead of a protective Gram-positive cell with a thicker peptidoglycan layer [33]. Thus, the antibacterial effect of the materials will depend on the type of interaction with these bacterial cells.

Concerning the lanthanoid cations, Eu^{3+} was chosen as a dopant agent to prepare two different doped $SrSnO_3$ perovskites with Eu^{3+} in Sr- or Sn-sublattice position - $(SrEu)SnO_3$ and $Sr(SnEu)O_3$ - by the possibility of obtaining different point defects, such as cationic/anionic vacancies and reduced cations in the $SrSnO_3$ perovskite lattice. Europium is a rare earth not found in nature as a free element. It possesses two oxidation states (Eu^{3+} and Eu^{2+}), where Eu^{3+} is the most stable. Eu^{3+} has a unique $4f^6$ shell structure and it presents potential use in luminescence [34] as in light-emitting diodes [35, 36] and optical thermometer [36]. Europium is the most reactive rare earth element but is relatively nontoxic than other heavy metals. Although some studies suggest that europium has no known significant biological role [37], other reports have demonstrated that europium is an excellent luminescent probe for biochemical or biomedical applications, mainly applied in luminescent cellular tissue image tracking and monitoring drug release. Moreover, Eu^{3+} can display excellent proangiogenic activity through ROS generation and activation of mitogen-activated protein kinase (MAPK), and it can mimic Ca to enhance bone regeneration [38]. Eu^{3+} ions have already been used to prepare other doped perovskites with antibacterial activity, such as $BaSnO_3$ and $CaSnO_3$ [20]. However, it is essential to mention that, in our work, a meagre Eu^{3+} doping percentage was used to prepare the Eu^{3+}-doped $SrSnO_3$ materials for antibacterial applications, which significantly impacted their biocide activity. It is important to highlight that such a study has not been previously reported in the literature.

2. Experimental section

2.1. Material preparation

A wide range of synthesis methods has been applied for the preparation of different nanoparticulate materials with antibacterial activity, namely co-precipitation [21,23,39], conventional hydrothermal method [40], green sol-gel based method [20] microwave-assisted solvothermal method [41], among others. In the present work,

$SrSnO_3$, $(Sr_{0.99}Eu_{0.01})SnO_3$ and $Sr(Sn_{0.99}Eu_{0.01})O_3$ were synthesised by a modified-Pechini method using cationic polymeric precursor solutions.

For the synthesis of the target materials, tin chloride ($SnCl_2 \cdot 2H_2O$, J.T.Backer), ammonium hydroxide (NH_4OH, Vetec), strontium nitrate ($Sr(NO_3)_2$, Vetec), europium oxide (Eu_2O_3, Alfa Aesar), citric acid monohydrate ($C_6H_8O_7 \cdot H_2O$, Cargill), and ethylene glycol ($C_2H_6O_2$, Acros) were used as starting materials. The solutions were prepared following the procedure previously presented in the literature [17].

The polymeric solutions were thermally treated in an air atmosphere at 300 °C for 1 h to obtain the precursor powders that were further calcined in air at different temperatures (400, 500, 600, and 700 °C) for 4 h to study the evolution of the crystallisation of the desired perovskite phase. Further information about this synthesis procedure can be found in our previous works [17, 42, 43, 44].

2.2. Material characterisation methods

The synthesised materials were characterised by an array of techniques, including X-ray powder diffraction (XRD), infrared (IR) spectroscopy, UV-Vis spectroscopy, photoluminescence (PL), field emission scanning electron microscopy (FE-SEM), high-resolution scanning-transmission electron microscopy (HR-STEM), Energy Dispersive X-Ray Analysis (EDX), Q-band electron paramagnetic resonance (EPR) spectroscopy, nitrogen adsorption/desorption measurements, and X-ray photoelectron spectroscopy (XPS). More details about the used characterisation techniques and the analysis conditions can be found in the supplementary material file†.

2.3. Bacteria and culture conditions

The antibacterial activity of the perovskite oxides was tested against two representative bacteria, namely, *E. coli* (ATTC 25922) and *S. aureus* (ATTC 25923). The direct contact method was used to investigate the antibacterial efficiency of the solid materials as described in previous work [45]. Bacteria were grown on a Müller-Hinton agar (MH) solution at pH 7.3 ± 0.1 in a bacteriologic incubator at 37 °C for 24 h. Control tests were performed in aqueous saline (0.85%) solution to evaluate the bacteria growth.

The test was carried out on a mixture of 2 mL of inoculum in 10−4 colony-forming units per mL (CFU/mL) of *S. aureus* and *E. coli* with approximately 2 mg of the materials ($SrSnO_3$ and Eu^{3+}-doped $SrSnO_3$). An aliquot of 200 μL was withdrawn and spread vertically, horizontally, and diagonally over the growth medium with a Drigalski loop on the Petri dish. The plate was kept in the microbiological oven for 24 h. Then, the CFUs were counted. The positive bacterial growth control (0.85% saline) was prepared to compare and verify the strains' viability. The tests were performed in triplicate for each material.

3. Results and discussion

The powder precursors for the three perovskite samples were first calcined at different temperatures and evaluated by conventional XRD, FT-IR, UV-Vis, and Photoluminescence (PL) spectroscopies to monitor the evolution of the short and long-range ordering during the crystallisation process and identify the best temperature to obtain the desired perovskite phase for further measurements and applications. Thus, the crystallisation of the three perovskite materials synthesised in this work - $SrSnO_3$, $(Sr_{0.99}Eu_{0.01})SnO_3$ and $Sr(Sn_{0.99}Eu_{0.01})O_3$ - was initially investigated by XRD, as presented in Figure 1. The XRD patterns (Figure 1a-c) show a long-range disordered phase for the samples calcined at temperatures below 600 °C. However, a small peak near $2\theta = 30°$ (112) assigned to the perovskite phase was apparent after calcination of the undoped-$SrSnO_3$ sample at 500 °C.

(Figure 1)

The beginning of the crystallisation to the desired perovskite phase depended on the material composition, which agrees with the distorted orthorhombic $SrSnO_3$ perovskite structure with a *Pbnm* space group (ICSD file number 188140) [46]. For $SrSnO_3$ (Figure 1a), crystalline perovskite was observed after calcination at 600 °C. At this temperature, the XRD pattern of $SrSnO_3$ displays narrow symmetrical peaks indicating a long-range structure order. In contrast, broader diffraction peaks were attained for the Eu^{3+}-doped samples (Figure 1b-c), and appreciable amounts of

orthorhombic $SrCO_3$ as secondary phase (ICSD file number 166088) [47] remain even after calcination at higher temperatures. The presence of $SrCO_3$ as a secondary phase is commonly observed in strontium-based perovskite samples synthesized by wet chemical methods, especially the modified-Pechini method [17]. The $SrCO_3$ phase was confirmed in all samples by infrared measurements shown in Figure 2a-c. For $Sr(Sn_{0.99}Eu_{0.01})O_3$ (Figure 1c), a small peak near 2θ = 30 °, indexed as the (112) reflection of the perovskite phase, is observed, indicating that long-range ordering started after calcination at 600 °C. In contrast, for $(Sr_{0.99}Eu_{0.01})SnO_3$ (Figure 1b) crystallisation only occurred at 700 °C. These results suggest that the Eu^{3+}-doping weakly inhibits the perovskite crystallisation.

The average crystallite size estimated for the samples calcined at 600 and 700 °C is presented in Table 1. For pristine $SrSnO_3$, the crystallite size increased as the calcination temperature increased. The nucleation of the perovskite crystallites is thermally activated, followed by their growth increases as the temperature increases. It is also observed that the addition of europium leads to a significant reduction in crystallite size, probably due to the greater difficulty of crystallisation and increase in structural disorder (as evident from the FWHM values of (112) reflection near 2θ = 31° in the XRD patterns) caused by the dopant.

Table 1 - Crystallite size of the samples calcined at 600 and 700 °C derived from Scherrer equation for the (112) reflection in the XRD patterns.

Sample	**Temperature (ºC)**	**FWHM (degree)**	**Crystallite size (nm)**
$SrSnO_3$	600	0.2342	42.3
$SrSnO_3$	700	0.1999	50.4
$Sr(Sn_{0.99}Eu_{0.01})O_3$	600	0.3543	24.8
$Sr(Sn_{0.99}Eu_{0.01})O_3$	700	0.3664	23.7
$(Sr_{0.99}Eu_{0.01})SnO_3$	700	0.4008	21.4

In our previous work [17], using synchrotron techniques (S-XRD and XANES) in synergism with DFT simulations, it was shown that when the $SrSnO_3$ perovskite is doped with Eu^{3+} cations, these species can occupy both Sr^{2+} and Sn^{4+} sites. However, when Eu^{3+} cations are incorporated, reduced Eu^{2+} cations are formed in response to the charge compensation mechanism, and these cations occupy only the Sr^{2+} sites. In addition, the incorporation of Eu^{3+} cations induces further structural distortion in the $SrSnO_3$ lattice (inter- and intraoctahedral distortion), which can play a vital role in charge separation and redox ability of the synthesized materials. The selectivity of europium doping in other perovskite materials has also been reported by different authors. For instance, Jyothi and Gopchandran [48] prepared $SrTiO_3$:Y^{3+},Eu^{3+} and $SrTiO_3$:La^{2+},Eu^{3+} phosphors by a solid-state reaction and observed, using Rietveld refinements, photoluminescence and Judd-Ofelt (J-O) analysis, that Eu^{3+} cations can be located at different crystallographic sites in the lattice. The authors evidenced that when Eu^{3+} cations enter at the Ti^{4+} sites, an increased local asymmetry is observed. Cortés-Adasme et al. [49] identified by Rietveld refinements that when a high concentration of dopant is used, Eu^{3+} cations can occupy both Sr^{2+} and Sn^{4+} sites in $SrSnO_3$ samples obtained by the sol-gel method. More recently, Gupta et al. [50, 51] evaluated the symmetry and structural changes of Eu^{3+}-doped $SrSnO_3$ and $CaSnO_3$ perovskites prepared by solid-state synthesis method. By using Rietveld XRD refinements and EXAFS measurements together with DFT calculations, the authors confirmed that Eu^{3+} ions are distributed at both Ca^{2+}/Sr^{2+} and Sn^{4+} sites in the stannates' lattice. Based on all these studies, the general formula for both suggested cationic substitutions could be given by $(Sr_{1-3x/2}Eu_x)SnO_{3-\delta}$ for Eu^{3+} entering at the Sr^{2+}-sites and $Sr(Sn_{1-x}Eu_x)O_{3-\delta}$ for Eu^{3+} at Sn^{4+}-sites.

Figure 2a-c shows the FT-IR spectra of all samples calcined at different temperatures. According to the literature, IR modes of an *AB*O_3-type perovskite compound are observed below 700 cm^{-1} [52]. In the *Pbnm* structured orthorhombic perovskites, as for $SrSnO_3$, 25 modes are IR active at Γ of the Brillouin zone, given by $\Gamma_{IR} = 9B_{1u} + 7B_{2u} + 9B_{3u}$ [52].

(Figure 2)

In the present work, few modes related to the perovskite structure were observed due to the detection limit of the mid-IR spectrophotometer. Broad IR bands are observed in all samples, whatever the heat treatment temperature. In the IR spectra of the samples calcined at 400 and 500 °C, bands assigned to carboxylate groups ($RCOO^-$) bonded to metals were observed at around 1630 and 1380 cm−1, as a consequence of the chelation between the carboxylic group of citric acid and the cations, and further polyesterification with ethylene glycol during the synthesis of the solutions [44]. The intensity of such bands decreases after calcination at a higher temperature, and their behaviour differs between the pristine and Eu^{3+}-doped $SrSnO_3$ samples.

The observed variation in the bands related to the ester groups indicates that different chelate complexes are formed as suggested by De Oliveira et al. [44]. After calcination at 500 °C, the spectral profile changes slightly, and the shoulder at around 1380 cm^{-1} corresponding to the C−O vibration of the ester groups disappears. The bands assigned to esters were not observed after heat treatment above 600 °C, indicating the elimination of the organic network. The IR bands observed at 1774, 1448, 1070, 859, and 668 cm^{-1} define the carbonate group in the form of $SrCO_3$ [53], being more intense for samples calcined below 600 °C. Evidently, treatment at 700 °C results in complete combustion of the ester groups and partial elimination of carbonate, especially in $SrSnO_3$ (Figure 2a). These results are in agreement with the XRD analysis. Furthermore, bands at 3400 cm^{-1} were observed in the spectra, which are related to OH^- groups from adsorbed water on the samples' surface.

As noted above, IR absorption modes of the perovskite structure occur below 800 cm^{-1}, and broad bands in this region of the IR spectra were evident for the samples calcined at lower temperatures. These bands become more intense and better resolved after calcination at 700 °C, indicating an increase in short-range order of the coordination polyhedral in the perovskites' lattice. According to literature, high intensity infrared bands vibrations of the SnO_3^{2-} groups are found in two different regions: 300-400 and 600-700 cm^{-1}. Stretching vibrations of the Sn−O bonds can be found at about 674/548 cm^{-1} [43] and 662/535 cm-1 [44] in $SrSnO_3$, while the same bands are found at 642/559 cm^{-1} in $CaSnO_3$ [54], and at 669/534 cm^{-1} in $BaSnO_3$ [55].

In this work, for the SrSnO3 sample calcined at temperatures lower than 600 °C, these bands were observed at around 689 and 549 cm^{-1} and were assigned to SnO6

octahedra, indicating the presence of considerable disorder in the structure. However, in the IR spectrum of SrSnO3 (Figure 2a) calcined at 700 °C, one single and strong band is observed at 667 cm^{-1} that is assigned to Sn−O stretching vibrations in the SnO_6 octahedra, suggesting an increase in local symmetry. These bands are slightly shifted for $(Sr_{0.99}Eu_{0.01})SnO_3$ (Figure 2b) and $Sr(Sn_{0.99}Eu_{0.01})O_3$ (Figure 2c), indicating a change in the octahedra symmetry induced by Eu^{3+}-doping. Similar behaviour in IR spectra was observed by De Oliveira et al. [44] in a $Sr(SnTi)O_3$ system, and octahedra symmetry changes as Ti replaces Sn in the lattice. Octahedral symmetry modifications have also been evidenced using IR spectroscopy by Alves et al. [54] in $(CaSr)SnO_3$, and by Vieira et al. [56] in Fe-doped $SrSnO_3$ perovskites.

The optical characteristics of the materials were investigated by UV-Vis spectroscopy and photoluminescence (PL), as shown in Figure 3 and 4, respectively. The absorption UV-Vis spectra (top graphics in Figure 3) of the various samples are very similar, showing a rapid increase in absorption, especially for the samples calcined at lower temperatures.

(Figure 3)

An intense absorption is observed for $SrSnO_3$ (Figure 3a) calcined at 400 °C, which may be related to the greater amount of ester groups from the organic matter produced by the transesterification reaction of the polymeric precursors, which remained in the sample as evidenced in IR spectra (Figure 2). The intensity of the absorption band below 350 nm (3.5 eV) in the UV spectra decreases when the samples are calcined at higher temperatures or when Eu^{3+} is added to the perovskite lattice (Figure 3b-c). A different feature is observed in the spectra of the samples calcined at 700 °C. At this temperature, the absorption spectra are essentially linear, which is characteristic of semiconductor materials, and such behaviour is mainly due to an increase in short-range structural ordering of the perovskite lattice as evidenced by the XRD and IR results, which was also presented in our previous studies [17].

The samples' optical band gap (E_g) was calculated from the absorption curves according to Tauc's method [57] as shown in the $(\alpha hv)^n$ *vs.* photon energy plots (middle and bottom graphics in Figure 3). According to the literature, SrSnO3 may present both indirect and direct band gaps, with n = 1/2 and 2, respectively [58]. Different authors

estimated the E_g values for $SrSnO_3$ based materials in the range between 4.00 to 4.56 eV [17, 59, 60], whereas the bulk $SrSnO_3$ with an orthorhombic structure presents a E_g = 4.1 eV. Because the materials calcined at 400 and 500 °C still present highly disordered structures with a large amount of organic matter in the composition, it is not reasonable to estimate the band gap for them. As a result, only the materials calcined at 600 and 700 °C were considered to estimate indirect and direct E_g. The corresponding E_g for the samples are indicated in Figure 3. Slightly smaller E_g values at 600 °C were observed for the Eu^{3+}-doped samples compared to the pristine $SrSnO_3$, possibly related to the induced electronic defects in the lattice. Furthermore, E_g increases as the calcination temperature increases, in agreement with the crystallisation process indicated by the conventional XRD and IR analysis. The increase of E_g at higher temperatures indicates a decrease in structural distortions and partial elimination of defects. This is especially true for the Eu^{3+}-doped $SrSnO_3$ samples after calcination at 700 °C, which showed an increased direct band gap value from 4.05 eV for the former pristine $SrSnO_3$ sample to 4.07 eV for $(Sr_{0.99}Eu_{0.01})SnO_3$ and 4.14 eV for $Sr(Sn_{0.99}Eu_{0.01})O_3$ systems, agreeing with our previous DFT simulations [17].

It is worth noting that the presence of $SrCO_3$ as an impurity phase does not influence the band gap of the major perovskite $SrSnO_3$ phase, as $SrCO_3$ presented larger E_g values ($E_{g(direct)}$ = 5.31 eV and $E_{g(indirect)}$ = 5.09 eV), Figure S1†, than those estimated for the pristine and Eu^{3+}-doped SrSnO3 samples. Similar behaviour was observed by Marquez-Herrera et al. [61] who showed that the presence of $SrCO_3$ in $SrTiO_3$ does not induce any variation in the band gap of the titanate perovskite. As $SrCO_3$ is an ionic compound with no semiconductor behaviour, any variation in the band structure of the main perovskite phase should not be expected, especially when $SrCO_3$ is present in a low amount, as in the samples calcined at 600 and 700 °C.

Based on the measurements presented above, it is very likely that Eu^{3+} cations are incorporated in the $SrSnO_3$ crystal lattice at both Sr- and Sn-sites, leading to changes in the band structure of the stannate perovskite. With the occupancy of Eu^{3+} ions at Sr^{2+}- and Sn^{4+}-sites, it is natural that different electronic defects are formed in the lattice, and the photoluminescent properties of the synthesised materials can be affected. When Eu^{3+} cations substitute Sr^{2+}, cationic vacancies can be formed in response to charge compensation mechanisms, while the Eu^{3+}/Sn^{4+} substitution is compensated especially by oxygen vacancies. Apart from these, the charge imbalance can also be compensated

by cationic reduction, such as Eu^{3+} to Eu^{2+} and/or Sn^{4+} to Sn^{2+}. The presence of such defects was evidenced by PL, EPR and XPS spectroscopy, as discussed below.

The room temperature PL spectra are presented in Figure 4a-c.

(Figure 4)

From the PL, it is possible to evaluate the doping effect on the short- and medium-range order/disorder in the perovskite's samples [62]. According to the literature, in $SrSnO_3$ type structure, the short-range order concerns the local environments of each cluster, and the medium-range order is related to the distortion among the clusters located in the network. In contrast, the long-range order refers to the three-dimensional periodic repetition of the clusters in the perovskite network [62]. The PL emission at different regions can be assigned to defects with varying energy levels inside the band gap [63]. Concerning perovskite oxide materials, broadband PL can be originated from shallow defects (whose energy states are close to the valence or conduction bands due to less distorted structures) and deep ones (with energy states closer to the middle of the band gap due to highly distorted structures) [42, 62, 63, 64, 65, 66, 67]. Different authors have evidenced the origin of deep and shallow defects in perovskites [17, 68, 69, 70]. However, Longo et al. [63, 65] postulated that deep defects lead to a less energetic green-yellow-red emission, while shallow defects lead to a more energetic violet-blue emission. These can be characterised by fitting the PL spectra using a series of Gaussian curves (Figure S2-4†).

As expected, room temperature broadband PL was observed for $SrSnO_3$ (Figure 4a) with a band centred at 580-620 nm (2.0 to 2.1 eV), typical of multiphotonic processes [42], and the profile was not significantly impacted by changing the calcination temperature. Broadband PL was also observed for the Eu^{3+}-doped samples, with emission at higher energy regions for the samples calcined at lower temperatures. As a consequence of this broadband characteristic, the emission of all samples was classified as originating from shallow or deep defects (Figure 4d and Table S1-2† in the SI) as described by Longo et al. [63, 65].

The presence of $SrCO_3$ does not affect the PL properties of the prepared materials because the energy of the excitation source in the PL analysis (λ = 350.8 nm

with E = 3.54 eV) is much lower than the band gap energy of $SrCO_3$ ($E_{g(indirect)}$ = 5.09 and $E_{g(direct)}$ = 5.31 eV). The increase of the calcination temperature may lead to various structural orders featured by the $SrSnO_3$ and Eu^{3+}-doped $SrSnO_3$ samples. For $SrSnO_3$, when it is calcined at a higher temperature, a highly crystalline perovskite phase is formed, which means that an increased structural short- and long-range order is achieved, giving rise to a less distorted structure. This behaviour agrees with IR spectra, which displayed two bands due to the presence of distorted [SnO_6] octahedra below 700 °C and a single IR band related to a single octahedra symmetry in the sample calcined at 700 °C. It is well-known that PL results from a balance among an order/disorder degree. Materials with high and low-ordered structures present low formation of recombination centres, indispensable for the observance of PL [63]. As the calcination temperature increases, an increase of structural order and, therefore, a decrease in the lattice distortions in $SrSnO_3$ takes place. As a result, low PL emission is attained. In addition, the PL band centre tends to be shifted in the visible light spectrum towards shorter wavelengths, eliminating the less energetic defects (deep defects), as observed in Table S2†. This behaviour agrees with the data reported by Longo et al. [63, 65] for other related perovskite materials. In addition to structural distortions in $SrSnO_3$, oxygen vacancies ($V_O^{\bullet}$) can be present in $SrSnO_3$ calcined at 700 °C, which may introduce energy sublevels in the band gap leading to PL emission. However, it is expected that a higher number of oxygen vacancies are present in the samples calcined below 700 °C, which favours PL. The decrease in PL observed in the samples calcined at higher temperatures may also be due to eliminating such defects. It is still important to note that the $SrSnO_3$ host material presents a higher structural order at high calcination temperatures, which may lead to a decrease in broadband PL emission.

For the Eu^{3+}-doped $SrSnO_3$ systems, more shallow defects were observed for the samples calcined at temperatures between 400 and 600 °C. On the other hand, a significant increase in the number of deep defects is observed after calcination at 700 °C, indicating a higher medium-range disorder. These results are in agreement with the Rietveld refinement previously reported [17], by which a more distorted structure was evidenced after Eu^{3+}-doping for $(Sr_{0.99}Eu_{0.01})SnO_3$ and $Sr(Sn_{0.99}Eu_{0.01})O_3$ as better represented by angle variation in the structures depicted in Figure 4e, which were constructed using the refined structural parameters and atomic positions reported in Chantelle et al. [17].

Although all the samples presented broadband emissions, two narrow photo-luminescence bands assigned to Eu^{3+} ions have been evidenced in the PL spectra of the Eu^{3+}-doped samples. According to literature, these bands are observed at 592 and 615 nm, which are attributed to the permitted electronic transition $^5D_0 \rightarrow {}^7F_1$ (magnetic dipole transition) and the forbidden transition $^5D_0 \rightarrow {}^7F_2$ (electric dipole transition), respectively. In contrast, the band at 565 nm for $SrSnO_3:Eu^{3+}$ was assigned to the $^5D_0 \rightarrow {}^7F_0$ transition [35, 36, 71, 72, 73]. In the present work, the Eu^{3+}-doped samples presented three peaks, superimposed to a broadband emission, at 590, 615, and 705 nm, which are assigned to the $^5D_0 \rightarrow {}^7F_1$, $^5D_0 \rightarrow {}^7F_2$, and $^5D_0 \rightarrow {}^7F_4$ transitions of Eu^{3+}, respectively (Figure 4b-c). The intensities of these transitions decrease with increasing calcination temperature, which confirms different short and medium-range structural distortions according to the calcination temperature and sample compositions, as illustrated in Figure 4e. These results are consistent with the data reported by Macedo et al. [66] and Oliveira et al. [67] on Eu^{3+}-doped $CaZrO_3$ perovskites. The smallest intensities of the peaks after calcination at 700 °C agree with the increase of the percentage of emission assigned to deep defects for Eu^{3+}-doped $SrSnO_3$, which is also related to the smaller band gap of these samples (Figure 3) and the broader peaks in the XRD pattern (Figure 1).

In addition to the usual PL, a hump feature is observed between 400 and 500 nm, especially for $(Sr_{0.99}Eu_{0.01})SnO_3$ (Figure 4b). According to the literature, luminescence from Eu^{2+} ions is in the UV-blue range that can be assigned to the $4f_65d^1 \rightarrow 4f_7(^8S_{7/2})$ transition, characterised by a broadband emission [74, 75]. It is also noted that the blueshift emission in the Eu^{3+}-doped samples decreases as the calcination temperature increases, indicative of the oxidation of Eu^{2+} to Eu^{3+}. The presence of other types of defects may trap a higher number of charge carriers leading to quenching in the luminescence of Eu^{2+}. Similar behaviour has been observed in other solid materials [74, 76, 75]. By XRD, IR, UV-vis and PL analysis, we identified that pristine and Eu^{3+}-doped samples should be calcined at 700 °C to obtain materials with high short- and long-range order, which allows not only a great reproducibility but also the formation of important point defects in the structure that can be responsible for a change in the antibacterial properties of the materials.

The presence of the aforementioned paramagnetic centres was evidenced using Q-band EPR spectroscopy measurements on the samples with the highest crystallinity, namely those obtained after calcination at 700 °C (Figure 5).

(Figure 5)

To investigate whether the impurity $SrCO_3$ phase has an effect on the $SrSnO_3$ lattice properties and on the incorporation of europium cations, $SrCO_3$ was also analysed by EPR (Figure S5†). As expected, $SrCO_3$ did not possess any EPR signal as compared to synthesised materials. The pristine $SrSnO_3$ shows two EPR signals with different g-values, 2.0043 and 1.9994, respectively. The signal at g = 1.9994 probably arises from the presence of F-centres created by the electrons trapped at (Oxygen) anion vacancies [17, 77], confirming the presence of defects in the structure, indicated by PL measurements. By doping the Sr^{2+} site with Eu^{3+}, $(Sr_{0.99}Eu_{0.01})SnO_3$, this signal disappears completely, giving rise to a comprehensive EPR signal superimposed to a very weak narrow signal with a g-value of 2.0028. When the Sn^{4+} site was doped with Eu^{3+} ions, $Sr(Sn_{0.99}Eu_{0.01})O_3$, only a broad EPR signal was observed. As mentioned earlier, doping the host $SrSnO_3$ with Eu^{3+} increases the crystal's disorder and the concentration of deep defects, which is probably the result of the observed broad EPR signal. Critically, the EPR measurements confirm that the broad EPR signal indicates the presence of Eu^{2+} ions in the $SrSnO_3$ host crystal, as indicated by the PL measurements.

Figure 6 shows each sample element's XPS surveys and the high-resolution XP scans. As expected, the XPS survey (Figure 6a) revealed that Sr, Sn, and O are present on the samples' surface, together with Eu in the doped samples. The high-resolution XP spectra of the Eu *3d* lines are shown in Figure 6b, and those of Sr *3d*, Sn *3d* and O *1s* lines are shown in Figure 6c-e. Moreover, to better understand the surface characteristics of the samples, a semi-quantitative analysis of the atomic concentration of the surface elements was also performed, as shown in Table 2.

(Figure 6)

Table 2 - Atomic concentration of the elements on the surface of the Perovskite particles obtained by XPS spectra.

	Atomic concentration (%)			
Samples	**Sr**	**Sn**	**O**	**Eu**
$SrSnO_3$	17.9	17.0	44.5	0
$(Sr_{0.99}Eu_{0.01})SnO_3$	14.9	15.6	37.6	0.2
$Sr(Sn_{0.99}Eu_{0.01})O_3$	18.9	18.7	45.9	0.2

The Sr *3d* (Figure 6c) and Sn *3d* spectra (Figure 6d) clearly show a peak variation according to the composition, suggesting different atomic concentration (as shown in Table 2) and multiple environments on the surface of the samples. Moreover, the change in the O*1s* spectra profiles (Figure 6e), especially in $(Sr_{0.99}Eu_{0.01})SnO_3$, suggests that the structural distortions affect the surface of the materials. Peak shifts to lower binding energy (BE) are observed in the Sr *3d* (Figure 6b), except for $(Sr_{0.99}Eu_{0.01})SnO_3$, and in the Sn *3d* (Figure 6c), as well as in the O *1s* (Figure 6d) spectra further suggest Eu^{3+}-doping is occurring at the Sr^{2+}- and Sn^{4+}-sites as proposed by XANES and S-XRD refinement data in our previously reported work [17]. The shift to higher BE observed in the Sr *3d* spectrum of $(Sr_{0.99}Eu_{0.01})SnO_3$ (Figure 10b) might be due to the strong influence of the surrounding Sr^{2+} cations induced by the Eu^{3+} incorporation at the Sr-site, besides the likely formation of Sr-vacancies (V_{Sr}'') due to Eu^{3+}/Sr^{2+} substitution as suggested by the Kröger-Vink notations below. Also, the formation of this defect type is consistent with the semi-quantitative estimation of the elements on the samples' surface (Table 2). Apart from the XPS signals of the target elements, the C 1*s* signal was observed in the XPS surveys. It is important to emphasize that such a signal's appearance results from the double-faced carbon tape fixed to the stainless-steel sample holder or also from the carbonate phase formed in the materials. Despite this, the lower intensity of the C 1*s* signal suggests that a very scarce amount of carbonate is present on the materials' surface.

Lanthanoid-doping can lead to the creation of oxygen vacancies and cationic vacancies and may induce a reduction of Sn^{4+} to Sn^{2+} species on the surface of the $SrSnO_3$:Eu materials as indicated by the higher intensity of the Sn^{2+} band after curve fitting. The formation of the different possible defects is represented in Equations (1) to (5), written according to the Kröger-Vink notation.

$$SnO \xrightarrow{SrSnO_3} Sn''_{Sn} + V_O^{\bullet\bullet} + O_O^x \quad (1)$$

$$Eu_2O_3 \xrightarrow{SrSnO_3} 2Eu'_{Sn} + V_O^{\bullet\bullet} + 3O_O^x \quad (2)$$

$$Eu_2O_3 \xrightarrow{SrSnO_3} 2Eu^{\bullet}_{Sr} + V''_{Sr} + 3O_O^x \quad (3)$$

$$EuO \xrightarrow{SrSnO_3} Eu^x_{Sr} + O_O^x \quad (4)$$

$$EuO \xrightarrow{SrSnO_3} Eu''_{Sn} + V_O^{\bullet\bullet} + O_O^x \quad (5)$$

The high intensity of the Sn *3d* and O *1s* peaks in the XPS spectra (Figure 6), compared to the Sr *3d* peaks, indicates that the surface is Sn2+ rich in agreement to a recent report by Honorio et al. [16]. The Sn *3d* XPS spectra can be fitted with two doublets (corresponding to Sn $3d_{3/2}$ and Sn $3d_{5/2}$ levels). This fitting reveals that both Sn^{4+} and Sn^{2+} are on the surface of the materials, as also seen in the ZrO_2@$SrSnO_3$ system [16]. This suggests that a partial reduction of Sn^{4+} occurred during synthesis due to the combustion of a large amount of organic matter in the precursor. Depending on the sample composition, the O *1s* spectra can be fitted by three or four peaks, which might be especially due to the different local ambient of the elements on the material's surface. The most intense peak in the O *1s* spectra is located near 530 eV and corresponds to lattice oxygen (O^{stru}) associated with Sn^{2+} and Sn^{4+} environments on the perovskite surface. The second intense peak near 531.4 eV may correspond to the samples' chemisorbed oxygen species associated with oxygen vacancies. We believe that the peak located at 530.8 - 531.4 eV is related to oxygen vacancies due to the formation of reduced Sn^{2+} species.

Moreover, the lower intensity of the peak at 530.8 eV observed for $Sr(Sn_{0.99}Eu_{0.01})O_3$ indicates that a lower amount of oxygen vacancies is present in this sample when compared to the others, which is in good agreement with the Q-band EPR results. The weak peaks with lower BE observed in the deconvoluted spectra were not

identified. Concerning the concentration of the elements (Table 2), the semiquantitative analysis confirmed that all the elements are present on the surface structure of the samples. A deficiency of Sr and Sn is evidenced, besides the presence of nonstoichiometric O expected from the synthesis conditions of Eu3+ incorporation into the lattice. Regarding the Eu^{3+} cations, atomic Eu content equal to 0.2% corresponds to approximately 0.01%mol present in both $(Sr_{0.99}Eu_{0.01})SnO_3$ and $Sr(Sn_{0.99}Eu_{0.01})O_3$ samples, which indicates that the targeted doping has been accurately achieved.

From the above-presented results, we evidenced the presence of different point defects in the materials. However, it is difficult to accurately give the general formula for each target material synthesised in this work. To make their understanding easier, we preferred to maintain the formula as $SrSnO_3$, $(Sr_{0.99}Eu_{0.01})SnO_3$ and $Sr(Sn_{0.99}Eu_{0.01})O_3$ in the following discussion.

The morphological characteristics of the perovskite particles were examined using FE-SEM. At the same time, the BET analysis was performed to determine the samples' specific surface area. These results are displayed in Figure 7 and 10, respectively.

(Figure 7)

The higher magnification FE-SEM images (on the right of Figure 7) show the formation of irregular and large aggregates consisting of pseudo-spherical nanoparticles with dimensions of around and less than 100 nm. $Sr(Sn_{0.99}Eu_{0.01})O_3$ sample also contains some elongated particles with a rodlike morphology, whose lengths are bigger than 100 nm. Further characterisation of the nanoparticles' morphology was performed by HR-STEM as observed in Figure 8 and Figure S6-8†. From the TEM images, it is possible to note that the pristine $SrSnO_3$ sample (Figure 8 and S6†) exhibits nanoparticles sporadically attached to nanowires as the $Sr(Sn_{0.99}Eu_{0.01})O_3$ sample (Figure S8† and S9†).

(Figure 8)

The particle morphologies formed in these samples might result from the different nucleation processes and, therefore, particle crystallisation after calcination, as evidenced in XRD. The small nanoparticles apparently tend to coalesce into larger agglomerates. However, some particles grow differently from a particular nucleus or from the agglomeration of various nucleation sites to crystallise into well-defined nanorods of different sizes. The nanoparticles' part has a cluster-like shaping, with the size of the individual nanoparticles under 10 nm. The nanowires have between 600 and 100 nm in length and between 10 and 50 nm in width. $SrSnO_3$ with rod-like morphology has already been observed in samples of different methods. [78, 79, 80, 81] Rod or wirelike particles can also be related to the presence of mixed $SrSnO_3$ and $SrCO_3$. Particularly, $(Sr_{0.99}Eu_{0.01})SnO_3$ sample displays only the formation of tightly packed nanoclusters of nanoparticles without traces of nanowires (Figure 8 and S7†). The TEM-EDX elemental mapping (Figure 9 and S9†) indicated the distribution of Sr, Sn, O and Eu throughout the $(Sr_{0.99}Eu_{0.01})SnO_3$ and $Sr(Sn_{0.99}Eu_{0.01})O_3$ materials. These results suggest that the target samples were successfully prepared. It is important to note that the particle morphology of the samples is consistent with BET results (Figure 10), indicating a low specific surface area for the samples.

(Figure 9)

(Figure 10)

The $Sr(Sn_{0.99}Eu_{0.01})O_3$ and $SrSnO_3$ samples have the largest surface areas (13.3 and 12.6 m^2/g, respectively) compared to $(Sr_{0.99}Eu_{0.01})SnO_3$ (8.1 m^2/g). Considering a density of 6.43 g/cm^3 [82], the particle sizes were calculated from the specific surface areas as 74.0, 70.1 and 115 nm for $SrSnO_3$, $Sr(Sn_{0.99}Eu_{0.01})O_3$ and $(Sr_{0.99}Eu_{0.01})SnO_3$, respectively, which are in good agreement with the FE-SEM observations. However, the formation of smaller nanoparticles was precisely evidenced by HR-STEM. The morphology and the low specific surface area observed in all samples might be related to the nucleation and particle growth processes during calcination.

Bacteria are classified as Gram-positive and Gram-negative, depending on the difference in cell wall architecture [83]. In this work, *S. aureus* and *E. coli* was selected

as Gram-positive and Gram-negative bacteria, respectively. The antibacterial activity of the pure and Eu-doped $SrSnO_3$ samples, calcined at 700 °C, was evaluated against these bacterial strains. The results obtained with the direct contact method are shown in Figure 11.

(Figure 11)

When the samples were tested against *S. aureus*, the antibacterial performance of the Eu-doped material was higher than that of the undoped $SrSnO_3$ perovskite, with the highest inhibitory effect (99.1%) observed for the $(Sr_{0.99}Eu_{0.01})SnO_3$ nanoparticles. On the other hand, when the materials were tested against *E. coli*, no meaningful antimicrobial effect was evidenced, irrespective of the composition of the material, with growth inhibition of only 4% observed for all samples. Images of the Petri dish (inset in Figure 11) show a significant amount of several *E. coli* bacteria and almost no *S. aureus* after treatment with $(Sr_{0.99}Eu_{0.01})SnO_3$ as an antibacterial agent. No inhibition of the bacteria growth was observed when the saline control solution was used in the test. These results may be related to the structural disorder and chemical properties of the pristine and Eu-doped $SrSnO_3$ perovskites previously discussed.

As $SrCO_3$ is present as an impurity phase in the samples calcined at 700 °C, we evaluated whether its presence affects the antibacterial activity of the synthesised materials. For this, the standard commercial compound $SrCO_3$ was tested against *S. aureus* under the same conditions used for the other materials. It was observed that $SrCO_3$ surprisingly favoured bacterial cell proliferation and growth (Figure S10†), suggesting that $SrCO_3$ might act as a source of nutrients for this bacteria strain.

According to Wang et al. [2], the surface charge potential of nanoparticles strongly influences bacterial adhesion, as it affects the electrostatic attraction when the charges on the material and bacterial cell membrane are different, which favour interactions. The cell wall of Gram-positive bacteria consists of a glycan peptide layer (≈ 30 nm). Neutral and acid polysaccharides mainly cover the peptide surface and many different biomolecules [84]. Conversely, the cell wall of Gram-negative bacteria presents a more complex membrane structure and composition. The peptide layer of the cell wall of Gram-negative bacteria is thinner (≈ 10 nm), and the outer surface of the cell has a membrane composed of proteins, lipopolysaccharides, and phospholipids. An

atypical feature of the outer membrane of Gram-negative bacteria is the asymmetrical distribution of lipids on the outer and inner faces of the bacteria membrane. The outer membrane face contains all lipopolysaccharides (LPS), while the inner one contains mostly phospholipids. LPS present a higher charge per unit area than phospholipids. Most of the present charge is anionic at neutral pH due to the presence of carboxyl and phosphoryl groups on the bacteria's surface. These groups can be ionised, which results in the charged external face that is highly interactive with cations present in the external medium [84, 39]. As a result, the particle surface of metal oxides may become electrostatically attracted to the charge of the bacteria surface. In this sense, the metal oxide nanoparticles can act on the cell membrane provoking cell wall damage, inhibiting bacterial growth, or inducing death of these microorganisms [2, 26].

Another factor responsible for inhibiting bacterial growth is the particle size that can induce cell death [39]. It is known that nanoparticles act when they contact bacterial cell walls. The interactions can be electrostatic, by Van der Waals forces, and/or via receptor-ligand interactions. Different surface reactions may interfere with metabolic pathways, inducing membrane shape and function changes such as enzyme inhibition, deactivating proteins, inducing oxidative stress, and others [9]. Some metal ions present in the oxide may also be gradually released into an aqueous medium and subsequently absorbed by cell membranes, which in turn leads to direct interactions with the functional groups of proteins and nucleic acids [9]. In addition, metal ions on the surface of oxide particles may interact with the bacteria membrane, leading to changes in its permeability and, thus, results in bacteria death [39].

Although the surface area (S_{BET}) is a factor that may affect antibacterial activity, it did not influence the material activity in the present case, as the sample with the larger agglomeration, which is formed with tightly packed nanoparticles, displayed increased antibacterial activity. Moreover, particles are bonded in larger aggregates, which reduces their penetration capability into the cell membrane. In the current work, the surface charge characteristics and the electronic species seem to play a more critical role. All samples display a negative surface at pH 7.3 and do not have a meaningful activity against *E. coli*, which is Gram-negative bacteria. At the same time, a better result was obtained against *S. aureus*, which is Gram-positive bacteria. It also seems that Sn^{2+} and Eu^{2+} cations and oxygen vacancies present on the materials impact the surface charge properties of the material and, therefore, the antibacterial activity.

According to the PCZ data (Figure 12), the $SrSnO_3$ and $(Sr_{0.99}Eu_{0.01})SnO_3$ the tested samples presented a high negative surface charge potential value of -29.8 and -28.6 mW in pH 7.3, respectively, enabling electrostatic interactions with bacterial cells. On the other hand, $Sr(Sn_{0.99}Eu_{0.01})O_3$ presented a less negative zeta potential at this pH, -10mW, in agreement with XPS and EPR results, which indicated that this sample contains a lower amount of oxygen vacancies and consequently a peak of lower intensity associated with chemisorbed oxygen species in O *1s* XP spectrum. This less negative surface is less favourable for the adsorption of *S. aureus*. However, there may be other mechanisms of interaction of the $(Sr_{0.99}Eu_{0.01})SnO_3$ with bacteria that might be sensitive to the presence of Eu ions, as the pure $SrSnO_3$ did not demonstrate any inhibition of bacteria growth, despite the highly negative surface potential. In addition, it is important to highlight that the presence of $SrCO_3$ in the sample composition does not improve the antibacterial properties of the main perovskite stannate phase.

(Figure 12)

Sudhaparimala [20] investigated the antibacterial effect of Eu-doped $MSnO_3$ (M = Ca, Ba) on *P. aeruginosa* and *S. aureus* strains. These authors reposted 50% toxicity for *S. aureus* and *P. aeruginosa* when barium stannate or calcium stannate doped with europium were used at a concentration of 600 μg. Antibacterial activity was improved by increasing the dopant concentration. These authors did not suggest a possible mechanism of action. Sharma et al. [85] reported the antibacterial activity of macrocyclic complexes with unusual oxidation states of the metal ions. Similarly, Fathi et al. [86] associated the antibacterial activity of a series of metal complexes with the redox activity of the complexes.

Indeed, selectively doping Eu^{3+} into the Sr^{2+}-site enhanced the negative surface charge, electronic defects (oxygen vacancies, reduced Eu^{2+} and Sn^{2+} species), and balanced structural order/disorder (intermediate inter-octahedral tilts). These characteristics appear to have enhanced the redox ability, which is key to improving the antibacterial properties of Eu^{3+}-doped $SrSnO_3$. To evaluate the relationship between the dependence of site-doping on the structural ordering and antibacterial properties of the materials, the highly disordered $(Sr_{0.99}Eu_{0.01})SnO_3$ sample calcined at 600 °C was also

tested (Figure S10†). This sample promoted an increased growth of the *S. aureus* bacteria in about 50% compared to the control saline solution. On the other hand, the standard $SrCO_3$ material induced an increased growth of about 100% for the same bacterial strain compared to the control solution. It is still important to point out that the amount of the pure standard $SrCO_3$ material employed in the antibacterial tests is much higher than the quantity of impurity present in the synthesised samples. This indicates that structural ordering is very important for improving antibacterial properties.

Based on all these facts, we believe that the main reason for the enhanced antibacterial efficiency observed for the $(Sr_{0.99}Eu_{0.01})SnO_3$ calcined at 700 °C is a defect-structure synergism occurring due to the site-selective doping of Eu^{3+} cations at the Sr^{2+}-site and the balanced structural order/disorder characteristics associated with the inter- and intraoctahedral distortions. The doping can inevitably promote different electronic defects (such as cationic vacancies, oxygen vacancies and cationic reduction), and the structural distortions may enhance charge mobility throughout the complex clusters of the type $[SnO_6]$ and $[SrO_9]/[EuO_9]$ associated with oxygen vacancies as well as the presence of mixed-valence cations in the perovskite lattice to, therefore, improve the redox reactions on the materials' surface. This can be confirmed by the lower activity observed for the highly disordered $(Sr_{0.99}Eu_{0.01})SnO_3$ sample calcined at 600 °C compared to the corresponding ordered sample calcined at 700 °C. From these observations, the general redox mechanism related to antibacterial activity observed for the $(Sr_{0.99}Eu_{0.01})SnO_3$ material can be simplified by the different states in the complex clusters, also written according to the Kröger-Vink notation as follows.

For Eu^{3+}/Sr^{2+} substitution, formation of defects is displayed in Equations (3) and (4), while oxygen vacancies are formed due to reduction of Sn^{4+} as shown in Equation (1). Sn^{4+} reduction may also occur as a compensation of Sr^{2+} replacement by Eu^{3+} as displayed in Equation (6):

$$Eu_2O_3 \xrightarrow{SrSnO_3} Eu_{Sr}^{\bullet} + Sn_{Sn}'' + 3O_O^x \qquad (6)$$

The presence of Eu and Sn in the material with different oxidation states may induce redox reactions with the bacteria and between the own Eu and Sn, as displayed in Equation (7):

$$2Eu_{Sr}^{\bullet} + Sn_{Sn}'' \xleftrightarrow{charge\ transfer} 2Eu_{Sr}^{x} + Sn_{Sn}'' \quad (7)$$

Considering that these cations are located at specific sites, the charge transfer reaction that occur among the coordination polyhedra in the perovskite lattice may be proposed as shown in Equation (8):

$$2[Eu_{Sr}O_9 \cdot V_O]^{\bullet} + [SnO_6]'' \xleftrightarrow{charge\ transfer} 2[Eu_{Sr}O_9]^{x} + [SnO_6]^{x} \quad (8)$$

This charge transfer mechanism is favoured by the intermediate inter-octahedral tilts among the [SnO_6] octahedra (represented in Figure 4e) that, in turn, will boost the antibacterial activity by the redox reactions in the interface between *S. aureus* and the ($Sr_{0.99}Eu_{0.01}$)SnO_3 surface, also promoted by the negative charge of this perovskite surface as indicated by the zeta potential value.

4. Conclusions

This study reported the effect of Eu doping on the structural, electronic, surface and interface properties of the $SrSnO_3$ perovskite, focusing on the doping site, as ($Sr_{0.99}Eu_{0.01}$)SnO_3 and $Sr(Sn_{0.99}Eu_{0.01})O_3$ and the impact of this on the antimicrobial activity. Pristine $SrSnO_3$ and Eu-doped nanoparticles were successfully prepared by the Pechini-modified method and carefully characterised. Punctual surface and bulk defects, as Sn^{2+} and oxygen vacancies, were detected by different techniques (especially XPS and EPR), giving rise to different surface charge potentials, depending on the site-selective doping. As a consequence, higher adsorption of the Gram-positive bacteria on the surface of ($Sr_{0.99}Eu_{0.01}$)SnO_3 nanoparticles seems to have occurred, favoured by the negative surface charge properties of this samples, besides the possible redox reactions, due to the highest amount of Sn^{2+} and oxygen vacancies, and presence of Eu^{2+} species on the surface. The results suggest that doping $SrSnO_3$ with Eu^{3+} at a particular site is crucial for promoting a specific type and amount of electronic surface charges to tune antibacterial properties. These findings provide essential aspects that will pave a new pathway for the future synthesis of other Eu-doped compounds for different

applications. Also, because of the properties induced by Eu doping, these materials can also be envisioned in biological/biomedical applications where perovskite materials are already utilised and where europium is not used yet.

Conflicts of interest

There are no conflicts to declare.

Acknowledgements

The authors acknowledge the Brazilian agencies CNPq/MCTIC, CT-INFRA/FINEP/MCTIC, and CAPES/MEC (finance code 001) for the financial support. André Menezes would also like to thank CNPq (Grant 232680/2014-0), PNPD/CAPES (Grant 88882.317938/2019-01) and FAPESQ/PB - SSECT (17/2022) for the awarded fellowships. Brendan J. Kennedy acknowledges the support of the Australian Research Council. Alexandra Ciorita and Arpad M. Rostas greatly acknowledge the Romanian Ministry of Research, Innovation and Digitalization, Core Program Project PN19 35 02 03.

References

[1] R. C. Moellering Jr, Discovering new antimicrobial agents, *International Journal of Antimicrobial Agents* 37 (2011) 2–9.
[2] L.Wang, C. Hu, L. Shao, The antimicrobial activity of nanoparticles: present situation and prospects for the future, *International Journal of Nanomedicine* 12 (2017) 1227.
[3] S. M. Dizaj, F. Lotfipour, M. Barzegar-Jalali, M. H. Zarrintan, K. Adibkia, Antimicrobial activity of the metals and metal oxide nanoparticles, *Materials Science and Engineering: C* 44 (2014) 278–284.
[4] R. Kumar, A. Umar, G. Kumar, H. S. Nalwa, Antimicrobial properties of ZnO nanomaterials: A review, *Ceramics International* 43 (2017) 3940–3961.
[5] S. Stankic, S. Suman, F. Haque, J. Vidic, Pure and multi metal oxide nanoparticles: synthesis, antibacterial and cytotoxic properties, *Journal of Nanobiotechnology* 14 (2016) 1–20.
[6] F. Ahmad, Y. Al-Douri, D. Kumar, S. Ahmad, Metal-oxide powder technology in biomedicine, in: Metal Oxide Powder Technologies, Elsevier, 2020, pp. 121–168.
[7] V. Stanić, S. B. Tanasković, Antibacterial activity of metal oxide nanoparticles, in: Nanotoxicity, Elsevier, 2020, pp. 241–274.

[8] M. Khan, M. R. Shaik, S. T. Khan, S. F. Adil, M. Kuniyil, M. Khan, A. A. Al-Warthan, M. R. H. Siddiqui, M. Nawaz Tahir, Enhanced antimicrobial activity of biofunctionalized zirconia nanoparticles, *ACS Omega* 5 (2020) 1987–1996.
[9] S. Shaikh, N. Nazam, S. M. D. Rizvi, K. Ahmad, M. H. Baig, E. J. Lee, I. Choi, Mechanistic insights into the antimicrobial actions of metallic nanoparticles and their implications for multidrug resistance, *International Journal of Molecular Sciences* 20 (2019) 2468.
[10] K. Gold, B. Slay, M. Knackstedt, A. K. Gaharwar, Antimicrobial activity of metal and metal-oxide based nanoparticles, *Advanced Therapeutics* 1 (2018) 1700033.
[11] J. Gong, T. Xu, Perovskite materials in biomedical applications, in: Revolution of Perovskite, Springer, 2020, pp. 95–116.
[12] X. Hu, Y. Tang, T. Xiao, J. Jiang, Z. Jia, D. Li, B. Li, L. Luo, Rapid synthesis of single-crystalline $SrSn(OH)_6$ nanowires and the performance of $SrSnO_3$ nanorods used as anode materials for Li-ion battery, *The Journal of Physical Chemistry C* 114 (2010) 947–952.
[13] T. Ishihara, H. Fujita, Y. Takita, Effects of Pt addition for $SrSnO_3$–WO_3 capacitive type sensor on NO detection at high temperature, *Sensors and Actuators B: Chemical* 52 (1998) 100–106.
[14] Y. Shimizu, M. Shimabukuro, H. Arai, T. Seiyama, Humiditysensitive characteristics of La^{3+}-doped and undoped $SrSnO_3$, *Journal of the Electrochemical Society* 136 (1989) 1206.
[15] B. Muthukutty, R. Karthik, S.-M. Chen, M. Abinaya, Designing novel perovskite-type strontium stannate $SrSnO_3$ and its potential as an electrode material for the enhanced sensing of anti-inflammatory drug mesalamine in biological samples, *New Journal of Chemistry* 43 (2019) 12264–12274.
[16] L. M. C. Honorio, A. L. M. de Oliveira, E. C. da Silva Filho, J. A. Osajima, A. Hakki, D. E. Macphee, I. M. G. dos Santos, Supporting the photocatalysts on ZrO_2: An effective way to enhance the photocatalytic activity of $SrSnO_3$, *Applied Surface Science* 528 (2020) 146991.
[17] L. Chantelle, A. L. Menezes de Oliveira, B. J. Kennedy, J. Maul, M. R. da Silva, T. M. Duarte, A. R. Albuquerque, J. R. Sambrano, R. Landers, M. Siu-Li, et al., Probing the site-selective doping in $SrSnO_3$:Eu oxides and its impact on the crystal and electronic structures using synchrotron radiation and DFT simulations, *Inorganic Chemistry* 59 (2020) 7666–7680.
[18] I. A. de Sousa Filho, L. R. Arana, G. Doungmo, C. K. Grisolia,H. Terrashke, I. T. Weber, $SrSnO_3$ /g-C_3N_4 and sunlight: Photocatalytic activity and toxicity of degradation by-products, *Journal of Environmental Chemical Engineering* 8 (2020) 103633.
[19] A. A. Bhat, M. B. Zaman, J. H. Malik, K. A. Malik, I. Assadullah, R. Tomar, Facile way of making hydrothermally synthesized crystalline $SrSnO_3$ perovskite nanorods suitable for blue leds and spintronic applications, *ACS Omega* 6 (2021) 16356–16363.
[20] S. Sudhaparimala, Effect of europium (III) oxide doping on the nanoscale ceramic stannates $MSnO_3$ of Ca, Ba upon photo luminescence, catalytic degradation, and anti-microbial activity–green approach, *Material Science* (2018) 185–196.

[21] M. A. Subhan, T. P. Rifat, P. C. Saha, M. Alam, A. M. Asiri, T. Raihan, A. K. Azad, W. Ghann, J. Uddin, M. M. Rahman, Photocatalytic, anti-bacterial performance and development of 2, 4-diaminophenylhydrazine chemical sensor probe based on ternary doped Ag:$SrSnO_3$ nanorods, *New Journal of Chemistry* 45 (2021) 1634–1650.
[22] R. Abirami, C. Kalaiselvi, L. Kungumadevi, T. Senthil, M. Kang, Synthesis and characterization of $ZnTiO_3$ and Ag doped $ZnTiO_3$ perovskite nanoparticles and their enhanced photocatalytic and antibacterial activity, *Journal of Solid State Chemistry* 281 (2020) 121019.
[23] A. A. Shah, A. Khan, S. Dwivedi, J. Musarrat, A. Azam, Antibacterial and antibiofilm activity of barium titanate nanoparticles, *Materials Letters* 229 (2018) 130–133.
[24] C. Singh, A. Wagle, M. Rakesh, Doped $LaCoO_3$ perovskite with Fe: A catalyst with potential antibacterial activity, *Vacuum* 146 (2017) 468–473.
[25] D. Dvoranová, V. Brezová, M. Mazúr, M. A. Malati, Investigations of metal-doped titanium dioxide photocatalysts, *Applied Catalysis B: Environmental* 37 (2002) 91–105.
[26] R. Venkatesh, N. Dhananjaya, M. Sateesh, J. S. Begum, S. Yashodha, H. Nagabhushana, C. Shivakumara, Effect of Li, Na, K cations on photoluminescence of $GdAlO_3:Eu^{3+}$ nanophosphor and study of Li cation on its antimicrobial activity, *Journal of Alloys and Compounds* 732 (2018) 725–739.
[27] T. Ma, X. Zhai, Y. Huang, M. Zhang, P. Li, Y. Du, Cerium ions crosslinked sodium alginate-carboxymethyl chitosan spheres with antibacterial activity for wound healing, *Journal of Rare Earths* 40 (2022) 1407–1416.
[28] S. N. Matussin, M. H. Harunsani, M. M. Khan, CeO_2 and CeO_2-based nanomaterials for photocatalytic, antioxidant and antimicrobial activities, *Journal of Rare Earths* (2022).
[29] W. Jiang, G. Zhang, L. Jie, G. Hongbing, S. Chunxiang, D. Haoran, L. Zhang, G. Zhongping, L. Yuguang, Synthesis, characteristics, and antibacterial activity of a rare-earth samarium/silver/titanium dioxide inorganic nanomaterials, *Journal of Rare Earths* 32 (2014) 727–732.
[30] X. Bo, L. Wang, Y. Zhao, Facile synthesis of $Ag/La_2O_2CO_3$ hierarchical micro/nanostructures for antibacterial activity and phosphate removal, *Journal of Rare Earths* 38 (2020) 1372–1378.
[31] M. Yang, J. Zhang, Y. Wei, J. Zhang, C. Tao, Recent advances in metal-organic framework-based materials for anti-staphylococcus aureus infection, *Nano Research* (2022) 1–23.
[32] M. Mueller, C. R. Tainter, Escherichia coli, 2022.
[33] Y. N. Slavin, J. Asnis, U. O. Häfeli, H. Bach, Metal nanoparticles: understanding the mechanisms behind antibacterial activity, *Journal of Nanobiotechnology* 15 (2017) 1–20.
[34] Y. Xu, G. Li, X. Guan, Y. Wei, M. Zhang, Synthesis, crystal structure and photoluminescence properties of novel double perovskite $La_2CaSnO_6:Eu^{3+}$ red-emitting phosphors, *Journal of Rare Earths* 40 (2022) 1682–1690.
[35] P. Du, J. Tang, W. Li, L. Luo, M. Runowski, Manipulating concentration quenching and thermal stability of Eu^{3+}-activated $NaYbF_4$ nanoparticles via phase

transition strategy toward diversified applications, *Materials Today Chemistry* 26 (2022) 101013.
[36] P. Du, J. Tang, W. Li, L. Luo, Exploiting the diverse photoluminescence behaviors of $NaLuF_4$:*x*Eu^{3+} nanoparticles and g-C_3N_4 to realize versatile applications in white light-emitting diode and optical thermometer, *Chemical Engineering Journal* 406 (2021) 127165.
[37] A. Ugale, T. N. Kalyani, S. J. Dhoble, Potential of europium and samarium β-diketonates as red-light emitters in organic light-emitting diodes, in: Lanthanide-Based Multifunctional Materials, Elsevier, 2018, pp. 59–97.
[38] J. Chang, X. Zhang, K. Dai, Bioactive materials for bone regeneration, Academic Press, 2020.
[39] C. O. de Lima, A. L. M. de Oliveira, L. Chantelle, E. C. Silva Filho, M. Jaber, M. G. Fonseca, Zn-doped mesoporous hydroxyapatites and their antimicrobial properties, *Colloids and Surfaces B: Biointerfaces* 198 (2021) 111471.
[40] C. Tamames-Tabar, E. Imbuluzqueta, N. Guillou, C. Serre, S. Miller, E. Elkaïm, P. Horcajada, M. Blanco-Prieto, A Zn azelate MOF:combining antibacterial effect, *CrystEngComm* 17 (2015) 456–462.
[41] R. D. Campos, A. L. M. de Oliveira, A. Rostas, A. C. Kuncser, C. Negrila, A.-C. Galca, C. Félix, L. R. C. Castellano, F. F. da Silva, I. M. G. dos Santos, TiO_2/ZIF-67 nanocomposites synthesized by the microwave-assisted solvothermal method: a correlation between the synthesis conditions and antimicrobial properties, *New Journal of Chemistry* (2022).
[42] A. L. M. de Oliveira, V. Bouquet, V. Dorcet, S. Ollivier, S. Députier, A. G. de Souza, M. Siu-Li, E. Longo, I. T.Weber, I. M. G. dos Santos, et al., Evolution of the structural and microstructural characteristics of $SrSn_{1-x}Ti_xO_3$ thin films under the influence of the composition, the substrate and the deposition method, *Surface and Coatings Technology* 313 (2017) 361–373.
[43] M. Alves, S. Souza, M. Silva, E. Paris, S. Lima, R. Gomes, E. Longo, A. de Souza, I. Garcia dos Santos, Thermal analysis applied in the crystallization study of $SrSnO_3$, *Journal of Thermal Analysis and Calorimetry* 97 (2009) 179–183.
[44] A. De Oliveira, M. Silva, H. Sales, E. Longo, A. Maia, A. Souza, I. Santos, Effect of the composition on the thermal behaviour of the $SrSn_{1-x}Ti_xO_3$ precursor prepared by the polymeric precursor method, *Journal of Thermal Analysis and Calorimetry* 114 (2013) 565–572.
[45] L.-Y. Zheng, J.-F. Zhu, Study on antimicrobial activity of chitosan with different molecular weights, *Carbohydrate Polymers* 54 (2003) 527–530.
[46] A. K. Prodjosantoso, Q. Zhou, B. J. Kennedy, Synchrotron X-ray diffraction study of the $Ba_{1-x}SrSnO_3$ solid solution, *Journal of Solid State Chemistry* 200 (2013) 241–245.
[47] S. M. Antao, I. Hassan, The orthorhombic structure of $CaCO_3$, $SrCO_3$, $PbCO_3$ and $BaCO_3$: linear structural trends, *The Canadian Mineralogist* 47 (2009) 1245–1255.
[48] G. Jyothi, K. Gopchandran, Compositional tuning and site selective excitations in $SrTiO_3$: Y^{3+}, Eu^{3+} red phosphors, *Dyes and Pigments* 149 (2018) 531–542.

[49] E. Cortés-Adasme, R. Castillo, S. Conejeros, M. Vega, J. Llanos, Behavior of Eu ions in $SrSnO_3$: Optical properties, XPS experiments and DFT calculations, *Journal of Alloys and Compounds* 771 (2019) 162–168.
[50] S. K. Gupta, K. Sudarshan, R. Gupta, B. Modak, A. Kumar, P. Modak, Structural changes from conventional $SrSnO_3$ to ruddlesden–popper Sr_2SnO_4 perovskites and its implication on photoluminescence and optoelectronic properties, *ACS Applied Electronic Materials* 4 (2022) 878–890.
[51] S. K. Gupta, B. Modak, D. Das, A. K. Yadav, P. Modak, A. K. Debnath, K. Sudarshan, Light harvesting from oxygen vacancies and a-and b-site dopants in $CaSnO_3$ perovskite through efficient photon utilization and local site engineering, *ACS Applied Electronic Materials* 3 (2021) 3256–3270.
[52] E. Moreira, J. Henriques, D. Azevedo, E. Caetano, V. Freire, E. Albuquerque, Structural, optoelectronic, infrared and raman spectra of orthorhombic $SrSnO_3$ from DFT calculations, *Journal of Solid State Chemistry* 184 (2011) 921–928.
[53] P. Lu, X. Hu, Y. Li, M. Zhang, X. Liu, Y. He, F. Dong, M. Fu, Z. Zhang, One-step preparation of a novel $SrCO_3/gC_3N_4$ nanocomposite and its application in selective adsorption of crystal violet, *RSC Advances* 8 (2018) 6315–6325.
[54] M. C. Alves, S. C. Souza, H. H. Lima, M. R. Nascimento, M. R. Silva, J. W. M. Espinosa, S. J. Lima, E. Longo, P. Pizani, L. E. Soledade, et al., Influence of the modifier on the short- and long-range disorder of stannate perovskites, *Journal of Alloys and Compounds* 476 (2009) 507–512.
[55] H. B. Sales, V. Bouquet, S. Députier, S. Ollivier, F. Gouttefangeas, M. Guilloux-Viry, V. Dorcet, I. T. Weber, A. G. de Souza, I. M. G. Dos Santos, $Sr_{1-x}Ba_xSnO_3$ system applied in the photocatalytic discoloration of an azo-dye, *Solid State Sciences* 28 (2014) 67–73.
[56] F. Vieira, A. Oliveira, D. Melo, S. Lima, E. Longo, A. Maia, A. Souza, I. Santos, Crystallization study of $SrSnO_3$:Fe, *Journal of Thermal Analysis and Calorimetry* 106 (2011) 507–512.
[57] J. Tauc, R. Grigorovici, A. Vancu, Optical properties and electronic structure of amorphous germanium, *Physica Status Solidi* (b) 15 (1966) 627–637.
[58] C.-H. Wang, B. J. Kennedy, A. L. Menezes de Oliveira, J. Polt, K. S. Knight, The impact of anion ordering on octahedra distortion and phase transitions in SrTaO2N and $BaTaO_2N$, *Acta Crystallographica Section B: Structural Science, Crystal Engineering and Materials* 73(2017) 389–398.
[59] Q. Gao, K. Li, L. Zhao, K. Zhang, H. Li, J. Zhang, Q. Liu, Wide-Range band-gap tuning and high electrical conductivity in La-and Pb-doped $SrSnO_3$ epitaxial films, *ACS Applied Materials & Interfaces* 11 (2019) 25605–25612.
[60] H. Mizoguchi, H. W. Eng, P. M. Woodward, Probing the electronic structures of ternary perovskite and pyrochlore oxides containing Sn^{4+} or Sb^{5+}, *Inorganic chemistry* 43 (2004) 1667–1680.
[61] A. Marquez-Herrera, V. M. Ovando-Medina, B. E. Castillo-Reyes, M. Melendez-Lira, M. Zapata-Torres, N. Saldana, A novel synthesis of $SrCO_3$-$SrTiO_3$ nanocomposites with high photocatalytic activity, *Journal of Nanoparticle Research* 16 (2014) 1–10.

[62] J. Bohnemann, R. Libanori, M. L. Moreira, E. Longo, High-efficient microwave synthesis and characterisation of $SrSnO_3$, *Chemical Engineering Journal* 155 (2009) 905–909.
[63] V. Longo, L. d. Cavalcante, A. De Figueiredo, L. Santos, E. Longo, J. A. Varela, J. R. Sambrano, C. A. Paskocimas, F. De Vicente, A. Hernandes, Highly intense violet-blue light emission at room temperature in structurally disordered $SrZrO_3$ powders, *Applied Physics Letters* 90 (2007) 091906.
[64] A. L. M. d. Oliveira, M. C. F. Alves, J. L. A. d. Nascimento, V. Bouquet, I. T. Weber, S. Deputier, M. Siu-Li, E. Longo, M. Guilloux-Viry, I. M. G. d. Santos, Photoluminescence in alkaline earth stannate thin films grown by physical and chemical methods, in: Functional Properties of Advanced Engineering Materials and Biomolecules, Springer, 2021, pp. 155–183.
[65] V. M. Longo, L. S. Cavalcante, M. G. Costa, M. L. Moreira, A. T. de Figueiredo, J. Andrés, J. A. Varela, E. Longo, First principles calculations on the origin of violet-blue and green light photoluminescence emission in $SrZrO_3$ and $SrTiO_3$ perovskites, *Theoretical Chemistry Accounts* 124 (2009) 385–394.
[66] W. C. Macedo, A. G. B. Junior, K. de Oliveira Rocha, A. E. de Souza Albas, A. M. Pires, S. R. Teixeira, E. Longo, Photoluminescence of Eu^{3+}-doped $CaZrO_3$ red-emitting phosphors synthesized via microwave-assisted hydrothermal method, *Materials Today Communications* 24 (2020) 100966.
[67] M. C. Oliveira, R. A. P. Ribeiro, L. Gracia, S. R. de Lazaro, M. de Assis, M. Oliva, I. L. V. Rosa, M. F. d. C. Gurgel, E. Longo, J. Andres, Experimental and theoretical study of the energetic, morphological, and photoluminescence properties of $CaZrO_3$:Eu^{3+}, *CrystEngComm* 20 (2018) 5519–5530.
[68] C. Berglund, H. Braun, Optical absorption in single-domain ferroelectric barium titanate, *Physical Review* 164 (1967) 790.
[69] E. Heifets, R. Eglitis, E. Kotomin, J. Maier, G. Borstel, Ab initio modeling of surface structure for $SrTiO_3$ perovskite crystals, *Physical Review B* 64 (2001) 235417.
[70] P. Ghosez, J.-P. Michenaud, X. Gonze, Dynamical atomic charges: The case of ABO_3 compounds, *Physical Review B* 58 (1998) 6224.
[71] Z. Lu, L. Chen, Y. Tang, Y. Li, Preparation and luminescence properties of Eu^{3+}-doped $MSnO_3$ (M = Ca, Sr and Ba) perovskite materials, *Journal of Alloys and Compounds* 387 (2005) L1–L4.
[72] S. Wang, M. Lu, G. Zhou, H. Zhang, Z. Yang, Systematic investigations into $SrSnO_3$ nanocrystals (II) photoluminescent properties of the as-synthesized nanocrystals, *Journal of Alloys and Compounds* 452 (2008) 432–434.
[73] D. Patel, B. Rajeswari, V. Sudarsan, R. Vatsa, R. Kadam, S. Kulshreshtha, Structural, luminescence and EPR studies on $SrSnO_3$ nanorods doped with europium ions, *Dalton Transactions* 41 (2012) 12023–12030.
[74] H. Li, Y. Wang, Effect of oxygen vacancies on the reduction of Eu^{3+} in $Mg_3Ca_3(PO_4)_4$ in air atmosphere, *Inorganic Chemistry* 56 (2017) 10396–10403.
[75] J. Xue, M. Song, H. M. Noh, S. H. Park, B. C. Choi, J. H. Kim, J. H. Jeong, P. Du, Achieving non-contact optical thermometer via inherently Eu^{2+}/Eu^{3+}-activated

$SrAl_2Si_2O_8$ phosphors prepared in air, *Journal of Alloys and Compounds* 843 (2020) 155858.
[76] H. Guo, Y. Wang, G. Li, J. Liu, P. Feng, D. Liu, Insights into excellent persistent luminescence and detecting trap distribution in $BaHfSi_3O_9:Eu^{2+}$, Pr^{3+}, *Journal of Materials Chemistry C* 5 (2017) 12090–12096.
[77] M. Muralidharan, V. Anbarasu, A. Elaya Perumal, K. Sivakumar, Room temperature ferromagnetism in Cr doped $SrSnO_3$ perovskite system, *Journal of Materials Science: Materials in Electronics* 28 (2017) 4125–4137.
[78] T. Alammar, I. Hamm, V. Grasmik, M. Wark, A.-V. Mudring, Microwave-assisted synthesis of perovskite $SrSnO_3$ nanocrystals in ionic liquids for photocatalytic applications, *Inorganic Chemistry* 56 (2017) 6920–6932.
[79] A. R. F. A. Teixeira, A. de Meireles Neris, E. Longo, J. R. de Carvalho Filho, A. Hakki, D. Macphee, I. M. G. dos Santos, $SrSnO_3$ perovskite obtained by the modified pechini method—insights about its photocatalytic activity, *Journal of Photochemistry and Photobiology A: Chemistry* 369 (2019) 181–188.
[80] T. Mohan, S. Kuppusamy, R. J. V. Michael, Tuning of structural and magnetic properties of $SrSnO_3$ nanorods in fabrication of blocking layers for enhanced performance of dye-sensitized solar cells, *ACS Omega* (2022).
[81] Z. Ghubish, R. Kamal, H. R. Mahmoud, M. Saif, H. Hafez, M. El-Kemary, Photocatalytic activation of Ag-doped $SrSnO_3$ nanorods under visible light for reduction of p-nitrophenol and methylene blue mineralization, *Journal of Materials Science: Materials in Electronics* 33 (2022) 24322–24339.
[82] P. Villars, Pauling file in: Inorganic solid phases, http://materials.springer.com/isp/crystallographic/docs/sd_1001834 (2016).
[83] D. Zerbib, Bacterial cell envelopes: Composition, architecture and origin, *Handbook of Electroporation* 25 (2017) 417–436.
[84] A. R. Brown, R. A. Gordon, S. N. Hyland, M. S. Siegrist, C. L. Grimes, Chemical biology tools for examining the bacterial cell wall, *Cell Chemical Biology* 27 (2020) 1052–1062.
[85] V. Sharma, V. K. Vashistha, D. K. Das, Biological and electrochemical studies of macrocyclic complexes of iron and cobalt, *Biointerface Research in Applied Chemistry* 11 (2020) 7393–7399.
[86] A. M. Fathi, H. S. Mandour, E. Hassane Anouar, Characteristics of multidentate schiff base ligand and its complexes using cyclic voltammetry, fluorescence, antimicrobial behavior and DFT calculations, *Journal of Molecular Structure* 1224 (2021) 129263.

Figure captions

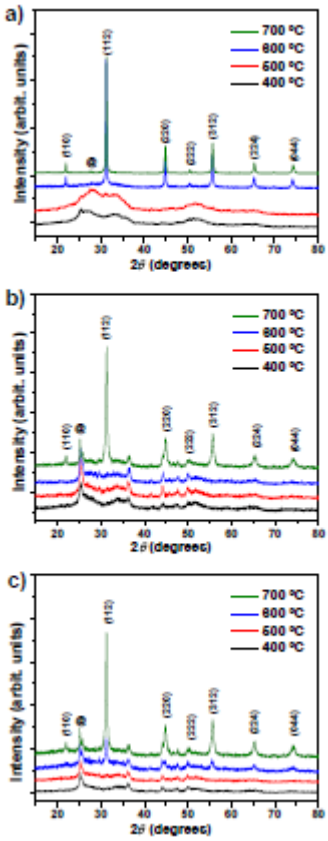

Figure 1: XRD patterns of the (a) $SrSnO_3$, (b) $(Sr_{0.99}Eu_{0.01})SnO_3$ and (c) $Sr(Sn_{0.99}Eu_{0.01})O_3$ samples calcined at different temperatures. The $SrCO_3$ most substantial peak near $2\theta = 25°$ is marked with @.

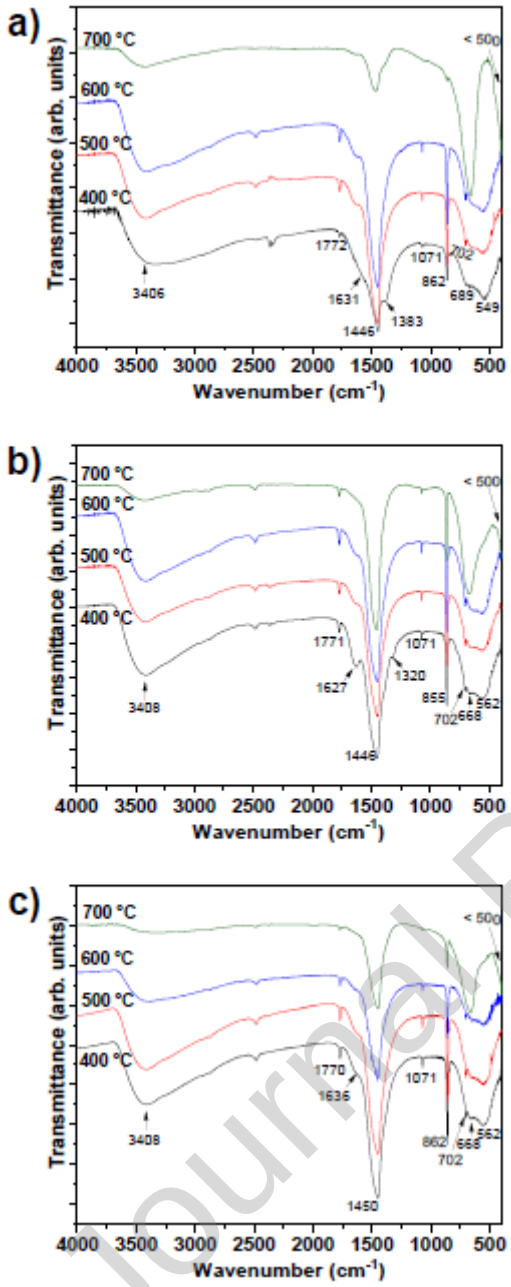

Figure 2: IR spectra of the $SrSnO_3$ (a), $(Sr_{0.99}Eu_{0.01})SnO_3$ (b) and $Sr(Sn_{0.99}Eu_{0.01})O_3$ (c) samples calcined at different temperatures.

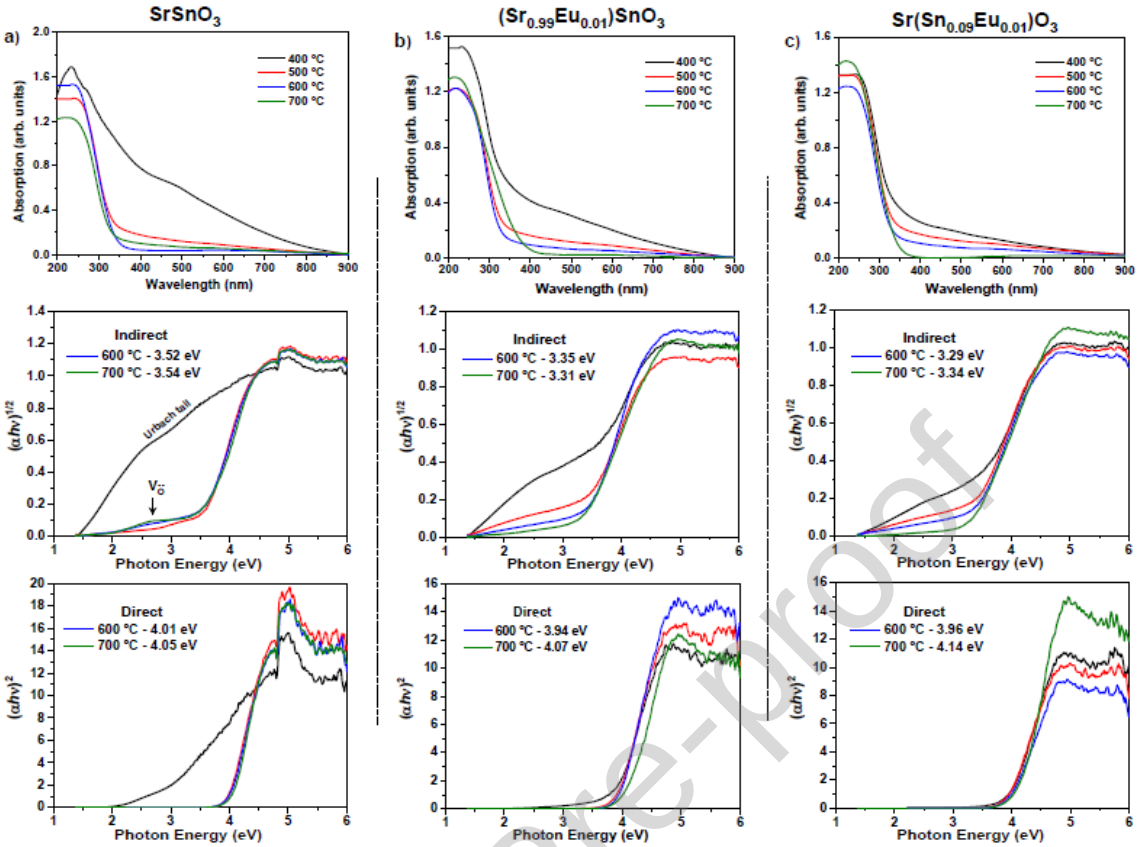

Figure 3: UV-Vis absorption spectra, $(\alpha h\nu)^{1/2}$ and $(\alpha h\nu)^2$ plots of the $SrSnO_3$ (a), $(Sr_{0.99}Eu_{0.01})SnO_3$ (b) and $Sr(Sn_{0.99}Eu_{0.01})O_3$ (c) samples after calcination between 400 and 700 °C. The corresponding E_g values are indicated.

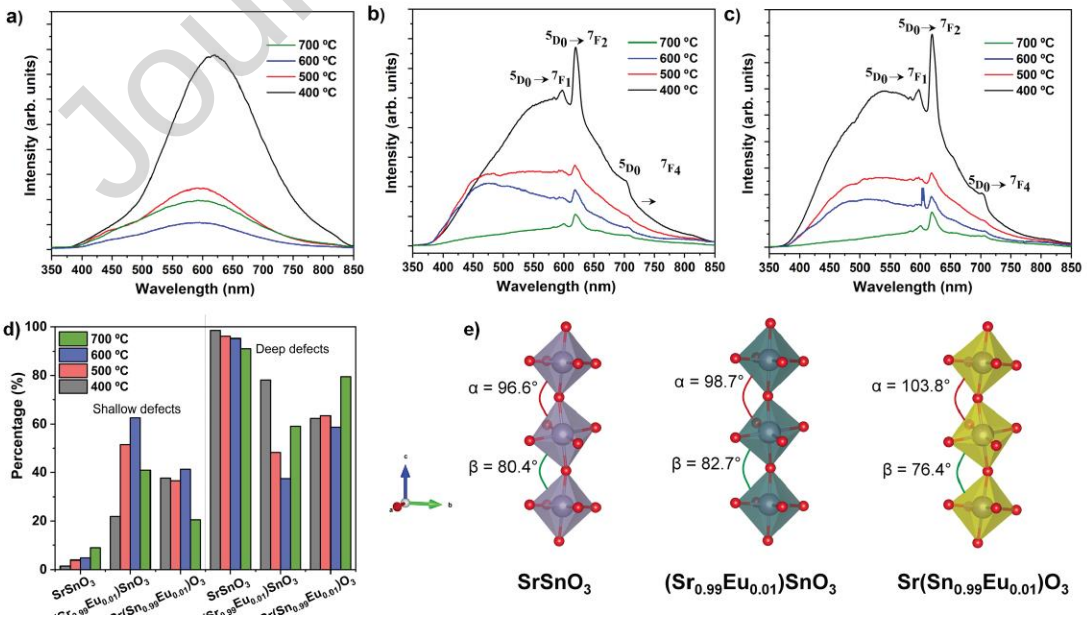

Figure 4: PL spectra of the $SrSnO_3$ (a), $(Sr_{0.99}Eu_{0.01})SnO_3$ (b) and $Sr(Sn_{0.99}Eu_{0.01})O_3$ (c) samples calcined at different temperatures; (d) Evaluation of the short-range disorder using PL (deep and shallow defects concentration) in $SrSnO_3$, $(Sr_{0.99}Eu_{0.01})SnO_3$ and $Sr(Sn_{0.99}Eu_{0.01})O_3$ samples calcined at different temperatures: *The shallow defects are calculated as the sum of the blue and green emission components and ** The deep defects are calculated as the sum of the yellow to red emission components. (e) Octahedral distortions, characterising medium-range structural disorder in $SrSnO_3$, $(Sr_{0.99}Eu_{0.01})SnO_3$ and $Sr(Sn_{0.99}Eu_{0.01})O_3$ crystal structures.

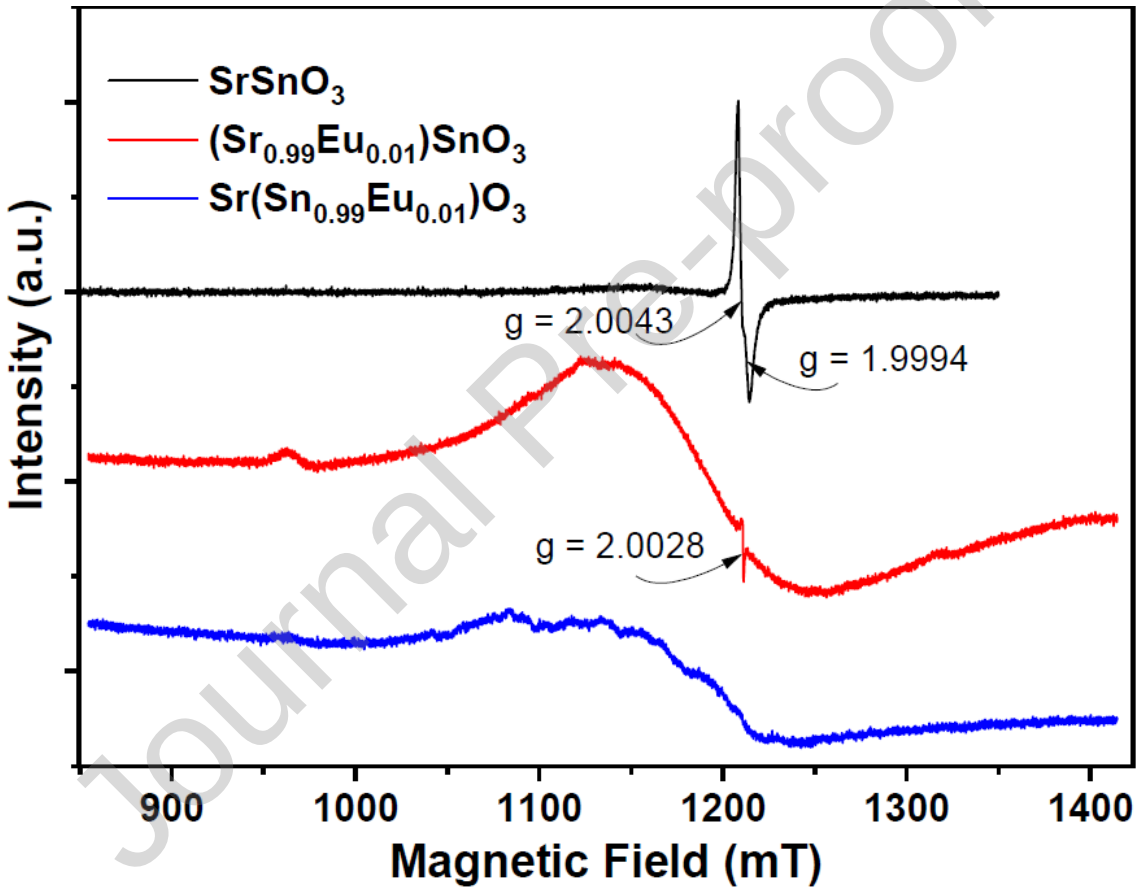

Figure 5: Q-band EPR spectra of the $SrSnO_3$, $(Sr_{0.99}Eu_{0.01})SnO_3$ and $Sr(Sn_{0.99}Eu_{0.01})O_3$ samples calcined at 700 °C, measured at room temperature.

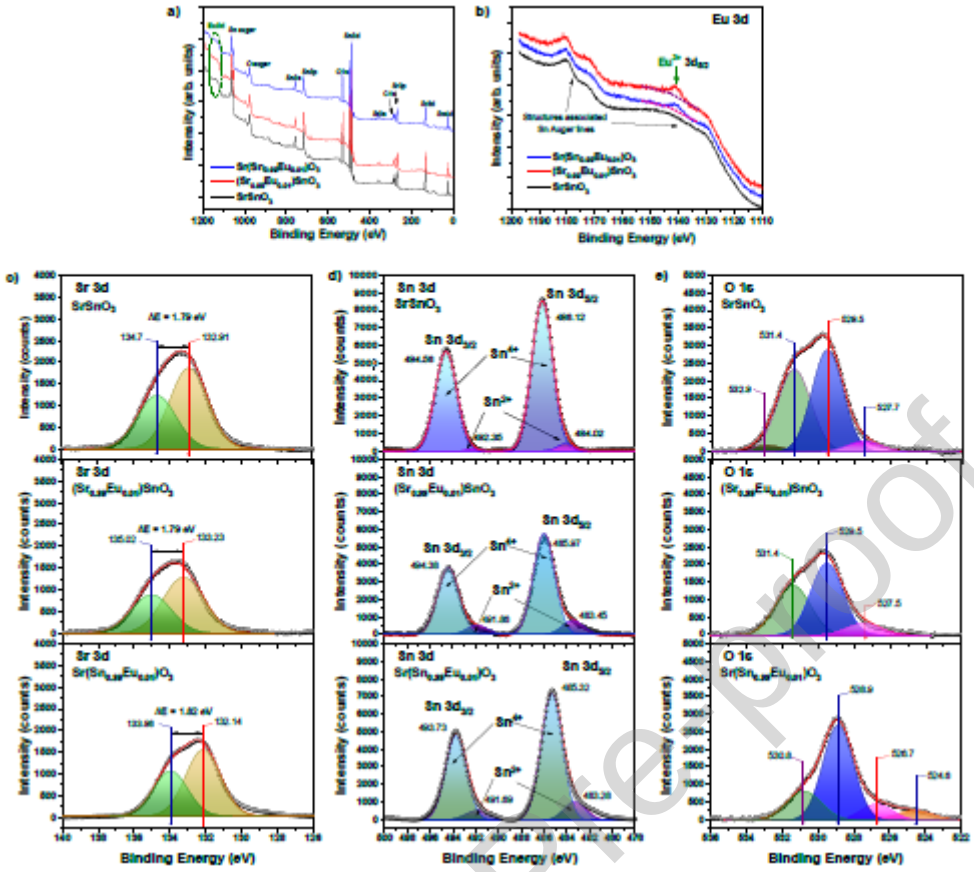

Figure 6: XPS spectra (a), high-resolution Eu 3d scan of the pure and Eu-doped $SrSnO_3$ samples. Fitting of the Sr 3d (c), Sn 3d (d), and O 1s (e) XPS spectra.

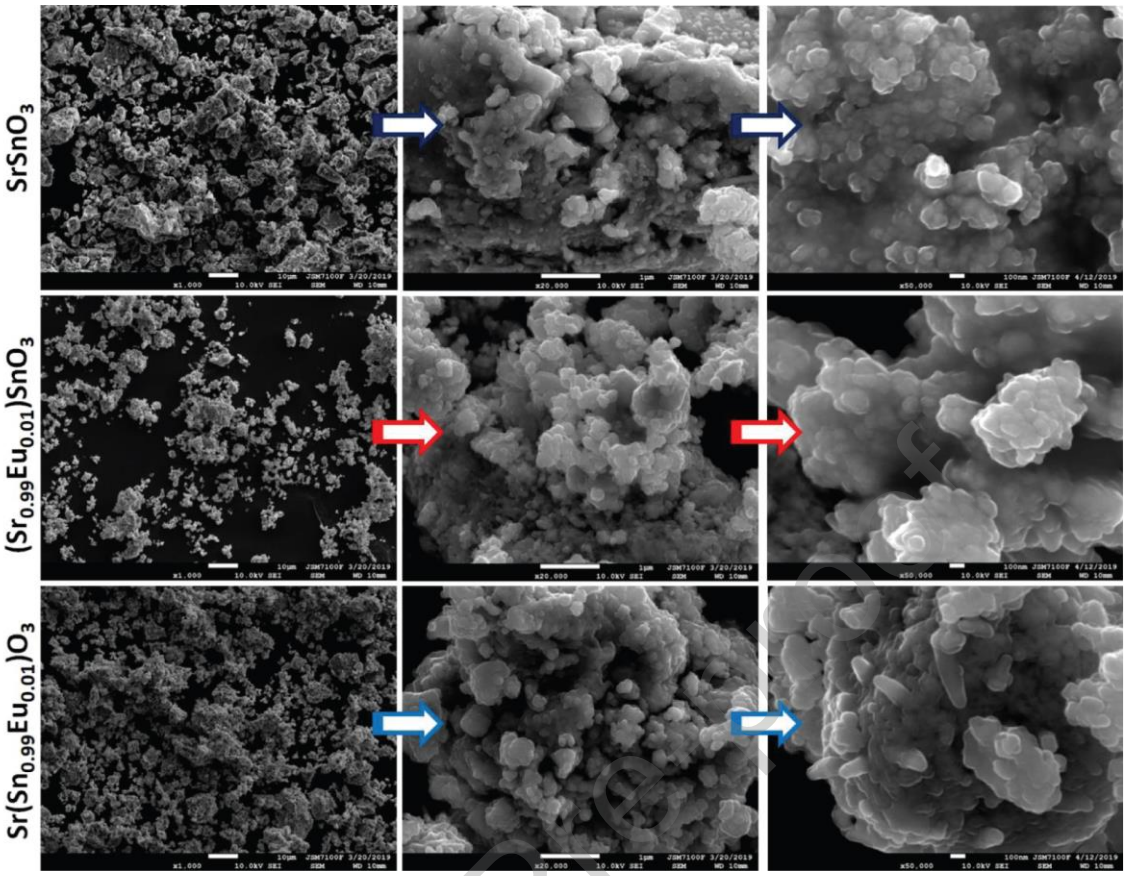

Figure 7: Low (left), middle (middle), and high (right) magnified FE-SEM images of the $SrSnO_3$, $(Sr_{0.99}Eu_{0.01})SnO_3$ and $Sr(Sn_{0.99}Eu_{0.01})O_3$ samples calcined at 700 °C.

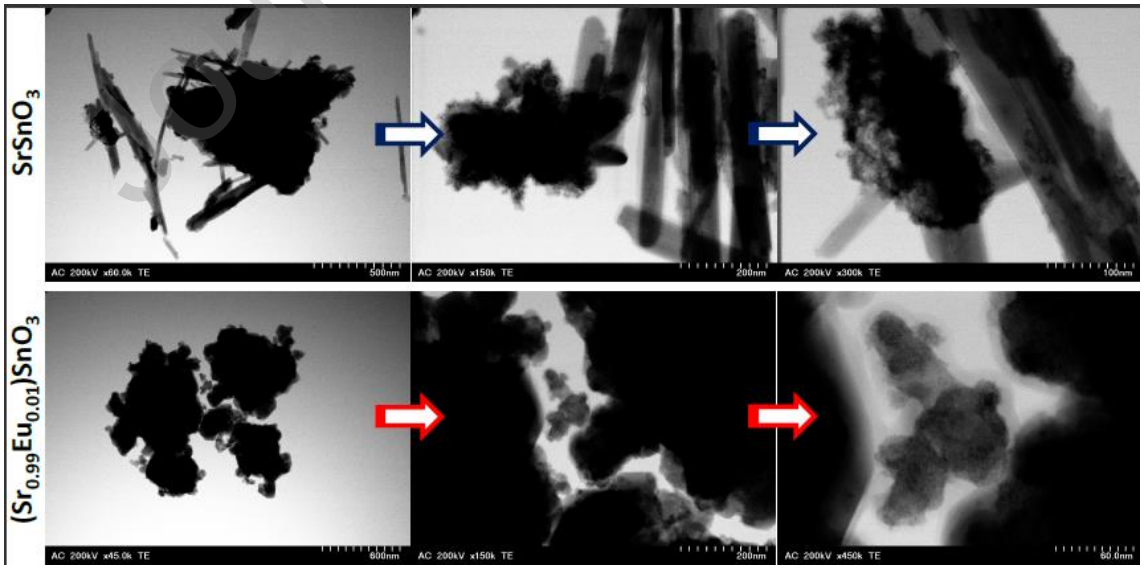

Figure 8: Low (left), middle (middle), and high (right) magnified TEM images of the $SrSnO_3$ and $(Sr_{0.99}Eu_{0.01})SnO_3$samples calcined at 700 °C.

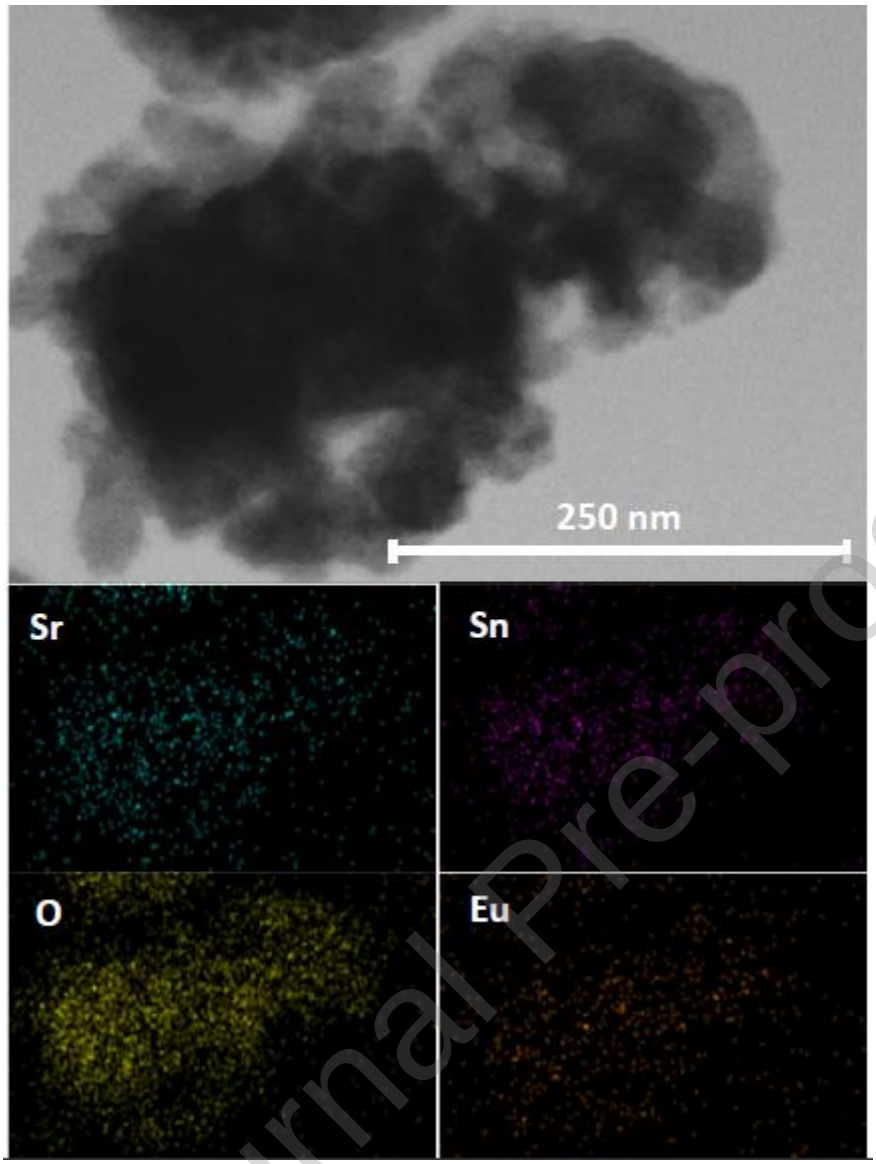

Figure 9: STEM-EDX elemental mapping of the $(Sr_{0.99}Eu_{0.01})SnO_3$sample calcined at 700 °C.

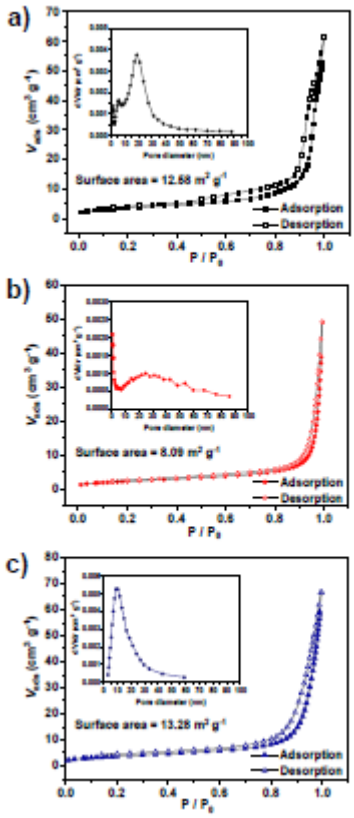

Figure 10: BET specific surface area calculated from nitrogen adsorption-desorption isotherms of the samples $SrSnO_3$ (a), $(Sr_{0.99}Eu_{0.01})SnO_3$ (b) and $Sr(Sn_{0.99}Eu_{0.01})O_3$ (c) calcined at 700 °C. The insets in the isotherm plot show the corresponding pore-size distribution.

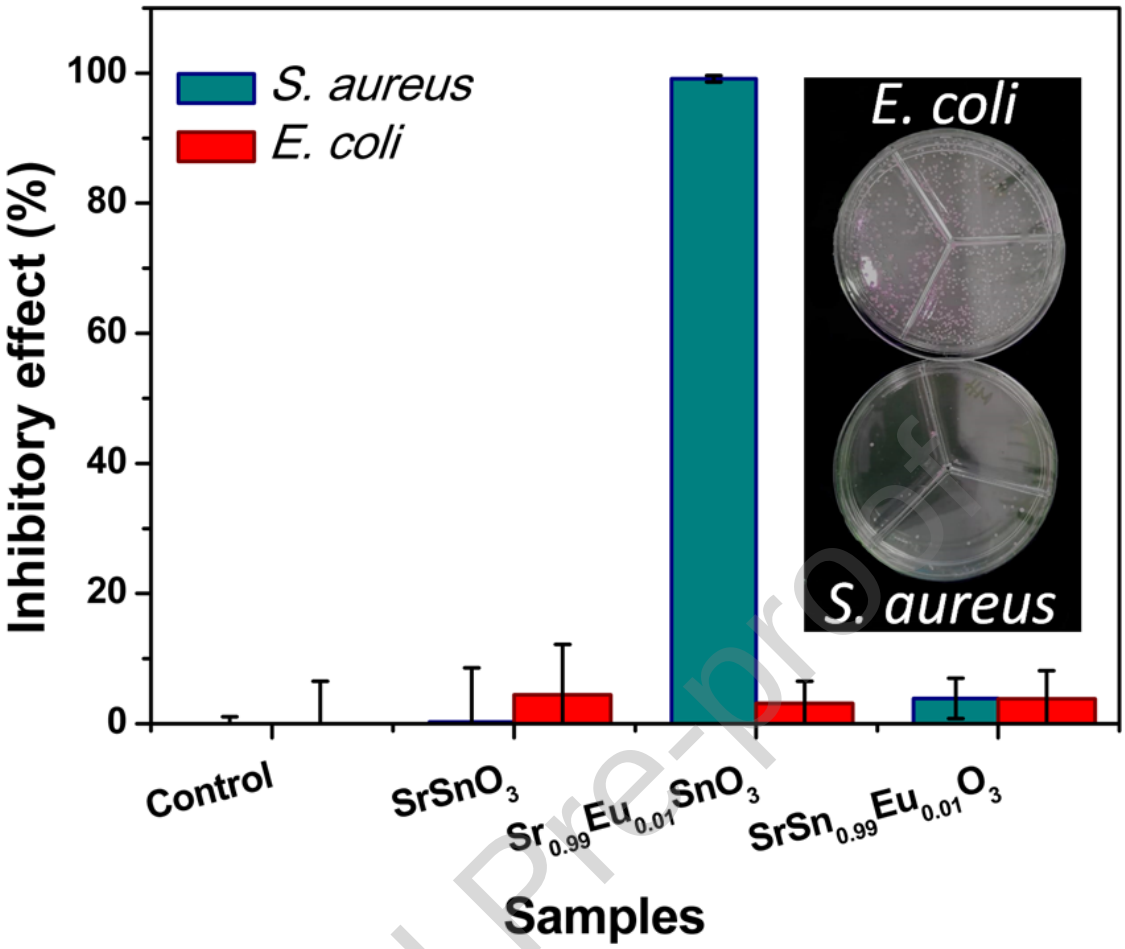

Figure 11: Bacterial growth inhibitory concentrations of the pure and Eu-doped $SrSnO_3$ samples. The inset shows the inhibitory effect of $(Sr_{0.99}Eu_{0.01})SnO_3$ particles on *E. coli* and *S. aureus.*

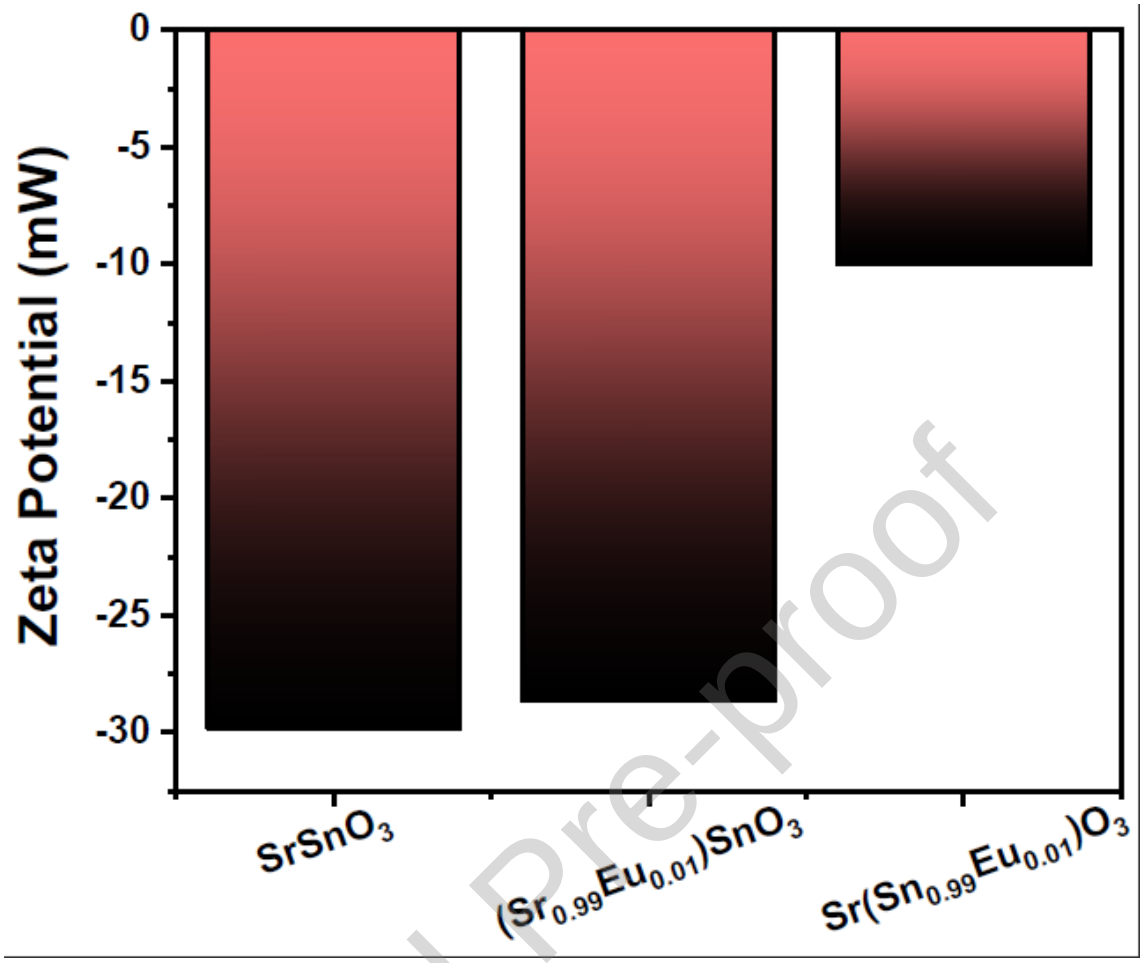

Figure 12: Zeta potential of the samples at pH 7.3.

Declaration of interests

☒ The authors declare that they have no known competing financial interests or personal relationships that could have appeared to influence the work reported in this paper.

☐ The authors declare the following financial interests/personal relationships which may be considered as potential competing interests:

Highlights

• Antibacterial activity of Eu-doped $SrSnO_3$-type materials depended on the site-doping.

• Antibacterial efficiency was correlated with the electronic defects on the material's surface.

• Incorporation of Eu into the $SrSnO_3$ lattice led to increased Sn^{2+} and oxygen vacancy defects on the surface.

• Eu-doped $SrSnO_3$ showed high selectivity for Gram-positive bacteria growth inhibition.